Flexible and Printed Electronics

Organic photodiodes: printing, coating, benchmarks, and applications

To cite this article: Noah Strobel *et al* 2019 *Flex. Print. Electron.* **4** 043001

Flexible and Printed Electronics

TOPICAL REVIEW

Organic photodiodes: printing, coating, benchmarks, and applications

Noah Strobel[1,2,4], **Mervin Seiberlich**[1,2,4], **Ralph Eckstein**[1,2], **Uli Lemmer**[1,2,3] **and Gerardo Hernandez-Sosa**[1,2]

[1] Light Technology Institute, Karlsruhe Institute of Technology, Engesserstr. 13, D-76131 Karlsruhe, Germany
[2] InnovationLab, Speyererstr. 4, D-69115 Heidelberg, Germany
[3] Institute of Microstructure Technology, Karlsruhe Institute of Technology, Hermann-von-Helmholtz-Platz 1, D-76344 Eggenstein-Leopoldshafen, Germany
[4] The authors contributed equally to this work.

E-mail: gerardo.sosa@kit.edu

Keywords: organic electronics, printing, coating, photodiode, photodetector

Supplementary material for this article is available online

OPEN ACCESS

RECEIVED
3 May 2019

REVISED
12 July 2019

ACCEPTED FOR PUBLICATION
12 November 2019

PUBLISHED
25 November 2019

Abstract

Organic photodiodes (OPDs) are set to enhance traditional optical detection technologies and open new fields of applications, through the addition of functionalities such as wavelength tunability, mechanical flexibility, light-weight or transparency. This, in combination with printing and coating technology will contribute to the development of cost-effective production methods for optical detection systems. In this review, we compile the current progress in the development of OPDs fabricated with the help of industrial relevant coating and printing techniques. We review their working principle and their figures-of-merit (FOM) highlighting the top device performances through a comparison of material systems and processing approaches. We place particular emphasis in discussing methodologies, processing steps and architectural design that lead to improved FOM. Finally, we survey the current applications of OPDs in which printing technology have enabled technological developments while discussing future trends and needs for improvement.

1. Introduction

Optical detectors are of paramount importance in modern technology as they are crucial sensing elements in fields like communications, imaging, medicine and consumer electronics. Currently, there is a rapidly increasing research interest in the development of photodetectors based on solution-processable organic materials [1–4]. These devices are set to complement traditional inorganic technologies based on Si, GaAs, or InP, where additional functionalities like mechanical flexibility, light-weight or transparency are opening new fields of application [5]. Furthermore, its solution processability allows for the potential of cost-efficient fabrication of integrated systems by printing or coating techniques [6–8]. In the last years, exciting proof-of-concept technologies and applications have been demonstrated in the fields of electronic skin, lab-on-chip, retina implants and stretchable electronics [9–15]. These exciting results highlight the potential impact of organic photo-detecting technologies for the fabrication of industrial, household and healthcare applications [10, 16–19].

Depending on its working principle or device architecture, photo-detecting technologies can be divided into different types such as photoresistors, phototransistors, or photodiodes.

Photoresistors offer a simple device architecture however they can only be operated under applied bias. Phototransistors present a way to tune sensitivity by a gate voltage, however, generally lack sufficient detection speed due to the lateral channel architecture resulting in long pathways for the collected charges [20]. In contrast, organic photodiodes (OPDs), offer an optimum balance between speed, response, linearity and processability and have thus been the object of focus of intense research by an increasing number of research groups in the last years [1, 4, 10, 20, 21]. A typical OPD device architecture and an example of an OPD array is presented in figure 1. The photoactive layer commonly comprised of a bulk-heterojunction (BHJ) of a donor and an acceptor semiconductor

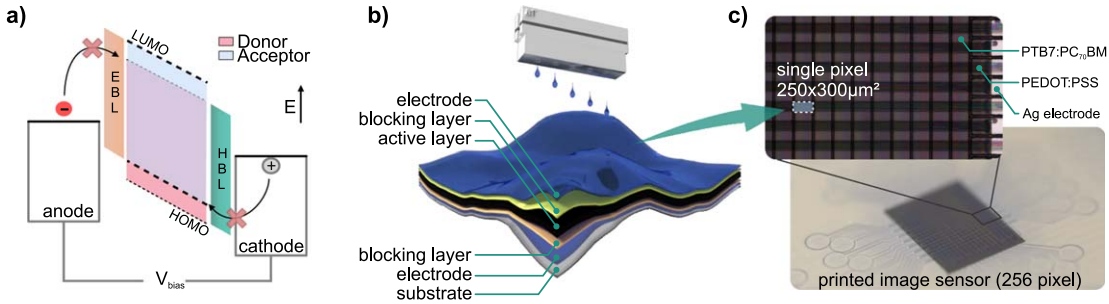

Figure 1. (a) Energy diagram of a typical organic photodiode (OPD) with electron- and hole blocking layers (EBL, HBL) aligned to the highest occupied molecular orbital (HOMO) and lowest unoccupied molecular orbital (LUMO) of the active layer. The active layer is typically fabricated from a donor–acceptor blend or bulk-heterojunction (BHJ). (b) Typical OPD device multilayer stack (c) Example of a printed image sensor with 256 pixels adapted with permission from [23], (CC-BY 2016).

material enables the photo electric conversion and thus predominantly defines the spectral responsivity ($R(\lambda)$) of the device. The interlayers are used to improve the energetic alignment of the electrode to the highest occupied molecular orbital (HOMO) or lowest unoccupied molecular orbital (LUMO) of the semiconductors. But more importantly they are used to minimize or block the injection of charge carriers from the electrodes during device operation. Lastly, the electrodes, of which at least one should be transparent in the spectral region of interest, are used to extract the generated charges. While in practice the energy diagrams of the HOMOs and LUMOs are a good starting point to investigate new device architectures, care should be taken when relating them to device performance as the final energy matching to the interlayers an electrodes may differ [22].

Historically, the development of OPDs has been performed hand-in-hand with the development of organic solar cells (OSCs) since both devices share the same underlying working principle and aim towards efficient photon-to-current conversion. Furthermore, both technologies share a large overlap in terms of active materials, electrodes and interlayers. The most efficient devices in each case have been achieved utilizing a BHJ-based active layer. However, the tremendous differences in their respective field of application demand for the optimization of particular characteristics of the employed materials, device architecture and/or processes. While OSCs rely strongly on matching the solar spectrum and maximize power conversion efficiencies, the OPD characteristics are tailored towards to the specific application field in terms of wavelength range, signal-to-noise ratio (SNR)or detection speed.

To date it is clear that solution-processed OPDs achieve comparable performance characteristics as inorganic devices [5]. Furthermore, novel and innovative device concepts have allowed to continuously push the limits of efficiency, narrow-band detection and infra-red response [3, 24]. However, to ensure technological relevance and commercialization readiness of a broad field of applications, the advances in device performance and functionality still require the development of versatile fabrication processes.

Printing and coating technologies offer a plethora of possibilities for the cost-effective fabrication of printed electronic devices [25–28]. Furthermore, these well-established conventional and digital techniques offer high-throughput and large-area processing, as well as high-resolution and full-freedom of design. The already proven industrial relevance of printing technologies together with its compatibility with roll-to-roll (R2R) and sheet-to-sheet (S2S) production processes show a great potential for the manufacturing of optical detection systems on the basis of OPDs. This has produced an increasing research effort in the processing of materials, development of printing processes and addressing of printing-related challenges for the demonstration of printable OPD architectures and its use as optical sensors.

In this review we compile the current progress in the development of OPDs fabricated exclusively with the help of industrial relevant coating and printing techniques. We review their working principle and figures-of-merit (FOM) highlighting the top device performances through a detailed comparison of material systems and processing technologies. Furthermore, we place particular emphasis in discussing methodologies, process development steps and architectural designs that resulted in improved FOMs. Finally, we survey the current applications of OPDs in which printing technologies have enabled technological developments and discuss future trends and needs for improvement. As such, we hope that this review serves both, researchers in the field as an overview of the state-of-the-art and remaining challenges as well as newcomers as an introduction to the basic principles and methods of OPD fabrication and characterization.

2. OPDs operation and figures of merit

Despite the common device architecture and physical working principle based in a donor–acceptor heterojunction, OSCs and OPDs differ fundamentally in

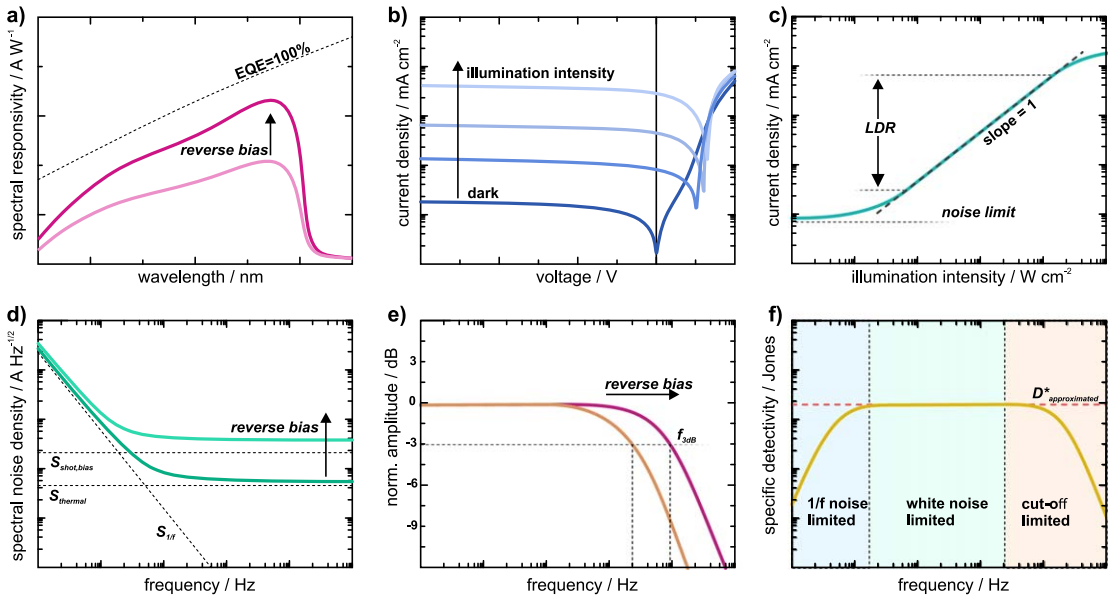

Figure 2. Schematic display of the OPD figures-of-merit and characteristics as a function of reverse bias or illumination intensity. (a) Spectral responsivity $R(\lambda)$, (b) J–V curve for different illumination intensities, (c) the linear dynamic range (*LDR*), (d) noise spectral density $S_{noise}(f)$ and its theoretical limits (shot-, thermal- and $1/f$-noise), (e) $R(\lambda)$ attenuation in dB as a function of excitation frequency. The −3 dB-cutoff frequency is marked as dotted line. (f) The frequency dependent specific detectivity D^* and the approximated frequency independent $D^*_{approximated}$ in different regimes of operation.

their way of operation [23]. While OSC FOMs are extracted from the forward bias regime, namely the photovoltaic mode, OPDs are typically driven at short circuit or reverse bias. The purpose of this operation mode is the effective enhancement of the specific OPD FOM, which are explained in detail in the following sections and are depicted schematically in figure 2. We want to emphasize that it is generally not possible to define a perfect OPD. In contrast to OSCs where high power conversion efficiency is the central goal, the key characteristics of OPDs strongly depend on its target application.

2.1. Spectral responsivity

The most basic FOM defining the application field of a photodetector is the spectral responsivity $R(\lambda)$. $R(\lambda)$ is defined by the generated photocurrent (I_p) per incident optical power (P_0) ,as a function of wavelength (λ) in units of AW^{-1}. The equation to calculate $R(\lambda)$ is given by:

$$R(\lambda) = \frac{I_p}{P_0} = \mathrm{EQE}\,\frac{e\lambda}{hc}, \qquad (1)$$

where e is the elementary charge, h is the Planck constant, c is the speed of light in vacuum and EQE the *external quantum efficiency*. The EQE represents the ratio of incident photons and collected charge carriers. This quantity is affected by the semiconductors molecular structure, active layer morphology and thickness, the choice of interlayers, absorption and recombination losses, as well as light in-coupling into the device.

An established routine for the measurement of $R(\lambda)$ involves the use of a lock-in-amplifier in combination with a monochromatic modulated light source of known frequency. The monochromatic light is typically provided by a light source with a broad illumination spectrum and a tunable monochromator. As depicted in figure 2(a), $R(\lambda)$ is usually enhanced by the application of a reverse bias since it allows for an increased electric field and faster charge extraction before recombination occurs. Furthermore, the use of bias light may have an effect on recombination processes that are often nonlinear with light intensity [29]. Its use should therefore be chosen depending on the final application and readers are encouraged to report its utilization in future publications for easier comparison between different OPDs.

2.2. Linear dynamic range (LDR)

The current output of an OPD typically increases with the intensity of the incident illumination as schematically shown in figure 2(b). The LDR represents the range of intensities where the current response of the OPD is linear with the incident optical power. The LDR is usually visualized by plotting the net photo current (after subtraction of the dark current) versus the light intensity in a double logarithmic plot and evaluated by fitting a linear function with the slope of unity (see figure 2(c)). The LDR is then calculated from the points of deviation from the linear dependency by the following equation:

$$\mathrm{LDR} = 20 \cdot \log \frac{i_{lin,\,max}}{i_{lin,\,min}}, \qquad (2)$$

where $i_{lin,\,max}$ and $i_{lin,\,min}$ are the highest and lowest currents where the deviation occurs. The factor 20 stems from the relationship between power and

current ($P \sim i^2$). Other definitions of the LDR are also used in literature, including the use of the dark current as the lower limit or by not subtracting the dark current from the photo current [2, 8].

In the high illumination intensity regime, the linear relationship is restricted by saturation effects stemming from carrier recombination losses due to higher charge densities in the device [30]. In contrast, the theoretical lower limit is set by the noise of the OPD which will be discussed in the following section.

2.3. Noise current in OPDs

The measured current output over time $i(t)$ of an OPD under a fixed illumination and reverse bias generally fluctuates around an average value i_{mean}. This statistical fluctuation is the so-called electronic noise and its rms-value is usually referred as the noise current i_{noise}. Electronic noise is present in all electronic devices and represents a strong limiting factor for the detection of weak signals in detectors. The electronic noise is commonly understood as the combination of three noise sources: (1) thermal noise resulting from thermal excitation of charge carriers, (2) shot noise due to their quantized nature leading to fluctuations in their distribution over time and space and (3) $1/f$-noise including the frequency dependent sources like contributions from the generation-recombination of electron–hole pairs.

While thermal and shot noise contributions are frequency independent (white noise), the other contributions show a characteristic $1/f$-frequency dependency [31–34]. The quantitative contribution of each of these noise sources at different frequencies f is given by the spectral noise densities in units of A Hz$^{-1/2}$:

$$S_{shot} = \sqrt{2ei_{dark}}, \tag{3.1}$$

$$S_{thermal} = \sqrt{4k_B T R_{shunt}^{-1}}, \tag{3.2}$$

$$S_{1/f} \propto \frac{1}{f}. \tag{3.3}$$

The parameters in the equations above are the elementary charge e, the dark current i_{dark}, the Boltzmann constant k_B, the temperature T and the shunt resistance of the OPD R_{shunt}. Note that at 0 V bias thermal noise will dominate while shot noise will rise when increasing dark current, i.e. higher reverse bias (see figure 2(d)).

As all contribution are statistically independent the total noise spectral density $S_{noise}(f)$ is given by:

$$S_{noise}(f) = \sqrt{S_{shot}^2 + S_{thermal}^2 + S_{1/f}^2(f)}\ . \tag{4}$$

For a given measurement system working in a defined frequency band B (i.e. range of measured frequencies), the noise current i_{noise} in units of A can be derived from the integral of the noise power (the square of $S_{noise}(f)$) over B:

$$i_{noise}^2(B) = \int_B S_{noise}^2(f)\, df\ . \tag{5}$$

Therefore, the noise current in a measurement system scales with the width of B which is termed the electrical bandwidth Δf. For frequency bands B, where the frequency dependent noise $S_{1/f}$ is neglectable, the white noise contributions dominate. This can be assumed for large bandwidths or when high-pass filters are employed. Only then is it possible to approximate $i_{noise}(B)$ from the bandwidth Δf:

$$\begin{aligned} i_{noise}(B) &\approx \sqrt{S_{shot}^2 + S_{thermal}^2}\ \sqrt{\Delta f} \\ &= \sqrt{2ei_{dark} + 4k_B T R_{shunt}^{-1}}\ \sqrt{\Delta f}. \end{aligned} \tag{6}$$

Moreover, under the condition that the shot noise current dominates over the thermal noise contribution, equation (6) can be further simplified and the noise can be calculated solely from the dark current. However, the false use of these approximations may lead to an underestimation of the noise and therefore needs to be considered carefully [30, 35]. To ensure the correct evaluation of the electronic noise in an OPD it is advised to perform a measurement of the noise, rather than calculating it from assumed noise sources.

There are several methods to measure the frequency dependent noise. One involves the measurement of the dark current over a period of time followed by performing a fast Fourier transform (FFT) of the signal in order to transform it in the frequency domain. Correct scaling factors to obtain the right unit as well as the use of suitable window functions like the Hann function need to be considered [36]. It is also possible to measure the noise spectrum directly with a spectrum analyzer or by a step by step evaluation of the signal magnitude at each frequency utilizing a lock-in amplifier with a defined electrical bandwidth [30, 35]. In all cases precautions are necessary to prevent the in-coupling of pick-up noise originating from surrounding sources. Therefore, the required amplification stage should be set up in close connection to the OPD in order to minimize in-coupling in the electrical wires. Furthermore, proper electromagnetic shielding of sample and voltage source might help to reduce unwanted signals.

2.4. Noise equivalent power and specific detectivity

$R(\lambda)$ alone is often not sufficient for the characterization of an OPD since it does not include information on the lower detection limit. For this purpose, the noise of the OPD has to be taken into account. A common parameter to describe the detection limit is the noise equivalent power (NEP in W Hz$^{-1/2}$), which corresponds to the incident optical power necessary to obtain a SNR of 1 when measuring at a 1 Hz electrical bandwidth. Note that reporting the NEP in units of Watts is not practical for the comparison of OPD performance as it is linked to the particular frequency band B of a specific measurement system.

The NEP is calculated from the frequency dependent spectral noise density $S_{noise}(f)$ described in equation (4) and is therefore generally frequency

dependent

$$\mathrm{NEP} = \frac{S_{noise}(f)}{R(\lambda)}. \tag{7}$$

The counterintuitive quantification of lower NEP for a better detector motivated Clark Jones to define the spectral detectivity (D) from the inverse of NEP as a parameter that describes the sensitivity of a detector [37, 38]. However, in order to define a FOM that enables a comparison across photodetectors with different dimensions D can be normalized by the device active area (A) to define the specific detectivity (D^*) given in units of Jones (cm $\mathrm{Hz}^{1/2}\,\mathrm{W}^{-1}$):

$$D^*(f, \lambda) = \frac{R(\lambda)\sqrt{A}}{S_{noise}(f)}. \tag{8}$$

The meaning of D^* corresponds to the achievable SNR for a 1 W signal, for a detector with 1 cm^2 active area measuring with an electrical bandwidth Δf of 1 Hz. The magnitude of D^* is a function of frequency and wavelength due to the frequency dependence of the spectral noise density $S_{noise}(f)$ and wavelength dependency of $R(\lambda)$. A schematic of the frequency dependence of D^* is presented in figure 2(f). Typically, D^* is limited in the low-frequency regime by $1/f$-noise while in the high frequency regime it is limited by the drop in $R(\lambda)$ due to the RC and transport limited detection speed (see following section). If the noise in the central frequency range is white (i.e. shot and thermally limited), a frequency independent D^* can be approximated for this regime using equation (6):

$$D^*(\lambda) \approx \frac{R(\lambda)\sqrt{A\,\Delta f}}{i_{noise}(B)} = \frac{R(\lambda)\sqrt{A}}{\sqrt{2ei_{dark} + 4k_B T R_{shunt}^{-1}}}. \tag{9}$$

However, the correct use of the approximation in equation (9) should be ensured as its incorrect use can lead to a considerable overestimation of D^*. In order to avoid misunderstandings in future publications, we suggest that details on the frequencies utilized for the evaluation of D^* should always be given.

2.5. 3 DB-bandwidth

For applications requiring a certain dynamic response, the detection speed of the OPDs is a crucial parameter. The FOM that quantifies the detection speed is the 3 dB bandwidth or cut-off frequency $f_{3\,\mathrm{dB}}$, which is defined by an attenuation of 50% in the output power (or 70% of the photocurrent) when the detector is illuminated by a light signal of increasing modulation frequency compared to that of the steady-state, i_0 (equation (10))

$$-3\ \mathrm{dB} = 20 \cdot \log \frac{i(f_{3\,\mathrm{dB}})}{i_0}. \tag{10}$$

There are two main limiting factors for the maximum detectable frequency of incident optical signals. The first one is the RC limited time constant t_{RC} (equation (11)) which rises from the total series resistance R_s of the device and the readout, and the capacitor-like geometry of the OPD formed by the active layer thickness d and the active area A

$$t_{RC} = R_s C = R\varepsilon\frac{A}{d}. \tag{11}$$

When aiming for high speed applications, smaller active areas and thicker active layers will reduce the junction capacitance and thus increase the RC limited cut-off frequency f_{RC}. Furthermore, the choice of the electrode material will have an impact on the total resistance and consequently on t_{RC} [35]. The second factor that limits the detection speed results from the transit time of the charge carriers resulting in a transit limited cutoff frequency f_{tr}. This parameter is influenced by the mobility of the charges and the thickness of the device. Furthermore, the presence of trapping effects can burden the detection speed especially for low light intensities. However, a reverse bias voltage can counteract the transit-limited charge extraction resulting in increased cut-off frequencies (see figure 2(e)). The total cut-off frequency is derived from both limits according to equation (12) [39]

$$\frac{1}{f_{3\,\mathrm{dB}}^2} = \frac{1}{f_{RC}^2} + \frac{1}{f_{tr}^2}. \tag{12}$$

As a general rule, the detection speed of the photodetector needs to be larger than the time scale of the signal to be monitored. For a large variety of applications, cut-off frequencies on the order of Hz are already sufficient. An example is represented by pulse oximetry, which is typically run with a sampling rate in the range tens or hundreds of Hz to switch between different wavelengths in order to cover the timescale of the heartbeat [12]. Similarly, for image sensor the bandwidth only has to be large enough to prevent image lag, typically in the order of 100 kHz [10, 15, 23]. However, for optical communication the detection speed directly limits data transmission rates and are therefore aimed to reach the highest possible cut-off in the high MHz or even GHz [16, 39].

3. Printing and coating techniques

Reporting record performances for devices fabricated by non-industrial-relevant fabrication techniques (e.g. spin coating), is useful to set a benchmark of new materials and OPD architectures [1, 4, 10, 20]. However, it overlooks the complexity of producing optoelectronic systems through printing or coating techniques. Especially, it underestimates the necessity of a printing-technique-specific ink formulation, the device architecture restrictions defined by the technique's working-principle, range of compatible solvents, substrate pretreatment or processing speed. Furthermore, it should be ensured that any approach employed to address these issues should not adversely affect the functionality of the printed layers but favor the intended material design.

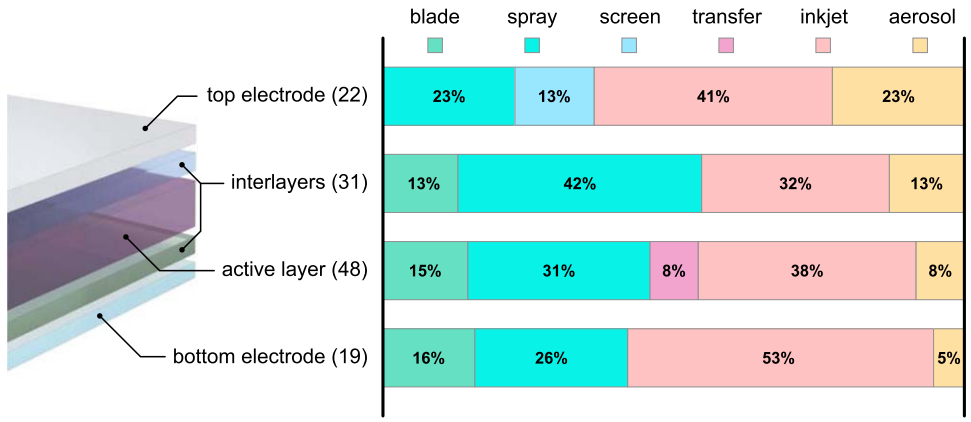

Figure 3. Usage of the different printing and coating techniques for the fabrication of the different OPD layers. The total number of reports per layer is included in parentheses.

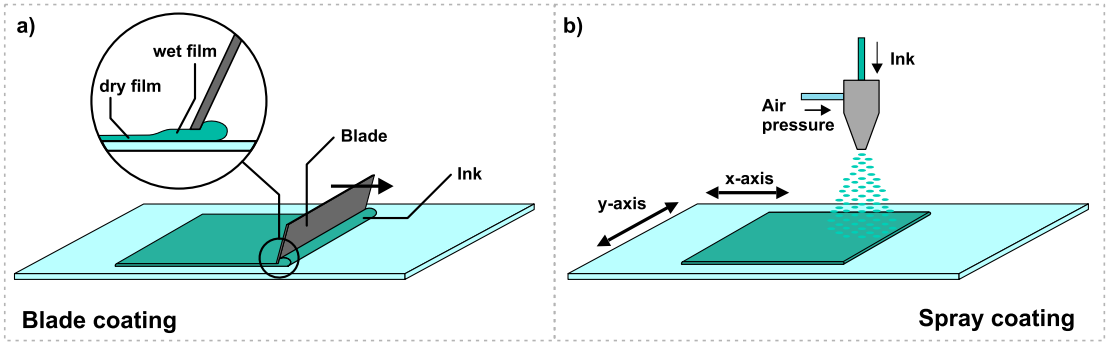

Figure 4. Coating techniques that have been employed for OPD layer fabrication. (a) Blade coating makes use of a blade or bar, which drags an ink continuously across a substrate, leaving a wet film that dries to form the desired layer. (b) Spray coating involves the generation of a tiny droplets which are deposited through a nozzle onto the substrate. 2D-deposition is possible through *x*–*y*-movement of the spraying apparatus or the substrate.

In the following section we introduce all the industrially relevant printing and coating techniques which have been employed in the past to partially or entirely fabricate OPDs. Each of the techniques have a unique working principle and are chosen depending on the requirements of the final application as it is discussed through this review. While all methods can arguably be described as 'coating techniques', we will utilize 'coating' as a synonym for non-structured film deposition and 'printing' when the deposition yields a patterned layer. We want to emphasize that one should not simply call a non-structured film deposition technique a printing technique as is sometimes misleadingly done in literature. We focused on detailing fabrication techniques that have the potential to be used in the industrial fabrication of solution processed applications and therefore lab-scale techniques such as spin coating, drop casting, brushing, or thermal evaporation are not included. Figure 3 gives an overview of the usage of the different techniques in literature, depicting how often they were applied to process the various layers of an OPD. It is evident that the active layer is by far the most processed layer and has the highest variety of techniques. Furthermore, a trend can be seen that indicates a pronounced utilization of printing techniques for electrodes whereas coating methods are more prominent for interlayers. This can be mainly attributed to the structuring capabilities of printing techniques, which represent a requirement for the electrode fabrication to define the active area of an OPD.

3.1. Coating techniques

In this review we understand coating techniques as methods which intrinsically lack the ability of structural deposition. For many applications where the fabrication of large areas is required they typically offer great advantages in terms of deposition speed, process simplicity and reproducibility. While the latter is especially true for lab-scale coating techniques like spin-coating, the device performance cannot be transferred easily to industrially relevant methods due to fundamental differences in the drying behavior in such a process. Therefore, any research performed on optoelectronic materials and devices directly deposited by industrial relevant coating techniques is highly valuable for the rapid translation of results from the laboratory towards commercial applications. Here we

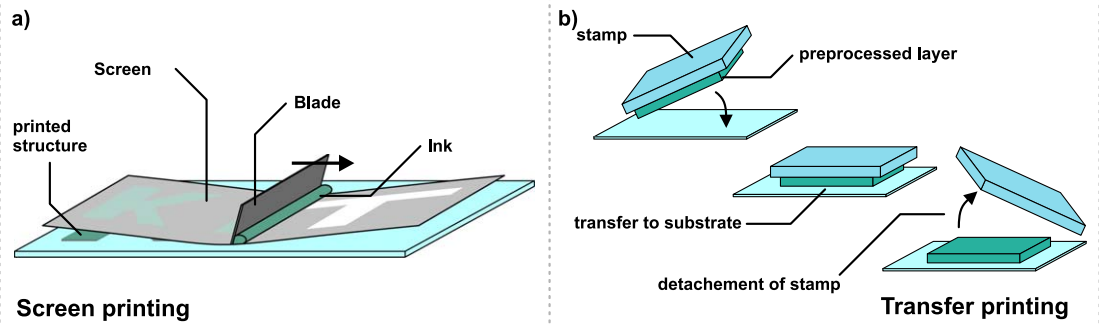

Figure 5. Traditional printing methods utilized for fabrication of layers in OPDs. (a) In screen printing a blade drags ink across a screen or mesh which is patterned with the desired layout. The ink is thereby deposited on the substrate only where the screen allows it. (b) Transfer printing makes use of a stamp on which the required dry layer is already preprocessed. By placing the stamp on the substrate and exerting some pressure and/or heat, the layer adheres to the substrate and the stamp can be detached subsequently.

detail the working principle of the two most common coating techniques for the processing of OPDs, blade- and spray coating (figure 4). For more details in these and other commonly used techniques in coating of organic electronics one could refer to literature [26].

3.1.1. Blade-coating

Blade-coating is a straight forward and fast coating technique which can be up-scaled from proof-of-concept laboratory systems to industrial R2R or S2S processes. While there are different variants of blade-coating, it generally requires a moving blade or bar, which continuously drags the ink over a flexible or rigid substrate. The process parameter-space of blade-coating comprises coating speed, gap or pressure to the substrate, substrate temperature and the rheological properties of the ink as well as drying conditions [40]. Counterintuitively, the film thickness increases for faster coating speeds. Blade-coating has the capability to reach deposition speeds $>10\,\mathrm{m\ s^{-1}}$ [41]. However, the dependence of the thickness on the speed has to be considered for the industrial implementation. A variation of the traditional bar-coating techniques used in high-throughput industrial production is Slot-die coating, which advantage is the continuous flow of ink that can be applied onto the substrate [26].

3.1.2. Spray-coating

Spray-coating is a technique that is widely applied in everyday industrial environments and is most commonly known for paint coatings. In this non-contact method, small ink droplets are conformably applied onto arbitrary surfaces via a carrier gas. There are several types, differentiable by the atomization methods and nozzle type [42]. The quality of the deposited film can be affected by the droplet-size, the distance to the substrate and the coating speed. An advantage of the spray-coating technique is the possibility to deposit layers with high thickness (on the μm scale) compared to other coating and printing techniques simply by increasing the spraying time. For OPDs this property is beneficial as thickness enhances light absorption and reduces leakage current. A challenge in spray-coating often lies in the optimization of the film roughness and thickness homogeneity in the nanometer scale [43].

3.2. Printing techniques

Since its invention, graphical printing has developed methods that are now considered standard in the production of printed materials such as newspapers, magazines or packaging. One of the main motivations for the use of printing technologies is that the initial equipment costs are rapidly offset by the possibility of printing high volumes on a short timescale [44, 45]. Therefore, the field of printed electronics aims to exploit this industrial profitability for the fabrication of applications in which high numbers or large areas are required. Below we present the main characteristics of printing techniques that have been utilized in the fabrication of OPDs.

3.2.1. Screen-printing

Screen printing (figure 5(a)) is a technique usually utilized for the deposition of thick films (up to ~500 μm). In electronics, it is an established method for the deposition of current collecting grids for Si photovoltaic devices. The basic screen printing process requires a mesh where the wire pitch and thickness determine the thickness and resolution of the printed pattern. The screen is placed at a distance from the substrate prior to dispensing the ink with the help of a rubber blade (or squeegee). This process step simultaneously fills the gaps in the mesh openings and bring the screen in contact with the substrate. The ink contained in the mesh openings is then transferred to the substrate to give place to the film formation and drying process. Commonly screen printing is found in a flat-bed or rotary architecture, this last being compatible with R2R printing at speeds up to 1000 m $\mathrm{min^{-1}}$ and feature-seizes of ~100 μm [46].

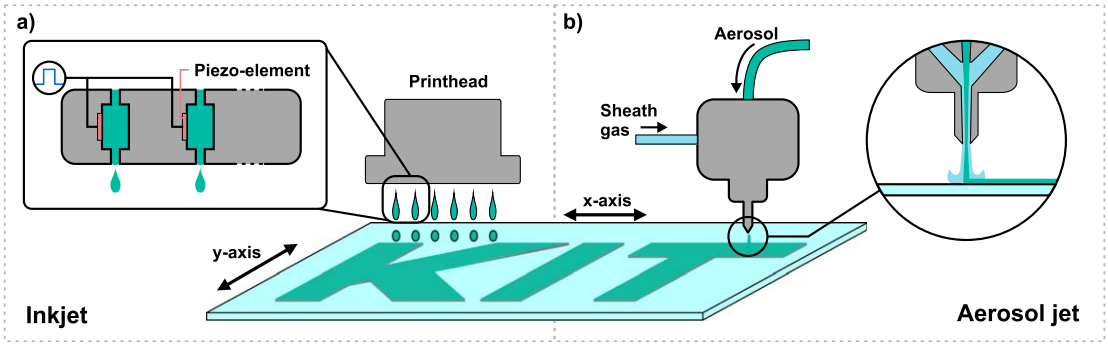

Figure 6. Schematic description of the functionality of digital printing techniques. (a) Inkjet printed structures are formed a pattern from adjacent single droplets that are being ejected from the nozzle head on demand. (b) Aerosol jet printing a high-resolution spray coating, Where an atomized ink is focused by a sheath gas stream. For both techniques either the printhead or substrate movement allows for 2D structuring.

3.2.2. Stamping and transfer processes

Several techniques allow the transfer of a pattern from one surface or substrate to another by the utilization of a stamp, release film, sacrificial layer or a contrast in surface free energy (figure 5(b)). These approaches are useful to avoid the direct or prolonged contact of non-orthogonal solvents to previously deposited layers, printing onto non-flexible substrates or depositing films onto 3D structures and curved surfaces. In many occasions these techniques are used in a lab-scale with the potential to be used in industrial relevant techniques such as transfer or pad printing.

3.3. Digital printing techniques

A great benefit of digital printing is the ability to freely design a desired layout by computer aided drawing software followed by a direct transfer of this layout to the printer. Thus, prescinding of the necessity of fabricating a printing form (e.g. engraved cylinder, cliché or mesh) as is done for traditional printing techniques considerably reduces the complexity of the process chain and therefore allows for a high degree of flexibility with great potential for rapid prototyping, low volume fabrication or personalized devices.

3.3.1. Inkjet printing

The most prominent digital printing technique utilized for the fabrication of a variety of organic electronic devices is inkjet printing. In this technique, the designed layout is formed by a 2D pattern of ink droplets, which are ejected from the nozzles of a printhead (see figure 6(a)). The pattern is typically calculated by the printing software and the necessary toolpaths for printhead and/or substrate holder are directly sent to the printer. The droplet ejection is enabled by consecutive filling and compression of the ink in the reservoir behind each nozzle. This is typically realized by feeding a transient voltage signal to a piezoelectric element. Aside from the viscoelastic properties of the ink (i.e. viscosity (~10 cP) and surface tension (~30–40 dynes cm^{-1})) [46], the waveform of this piezo signal as well as the print head temperature are the most important processing parameters that can be adjusted to control the drop shape, drop size, ejection speed and ejection frequency. Once the droplets are successfully ejected from the printhead, additional measures have to be taken to provide a desirable layer formation. Depending on the wetting behavior of the ink on the substrate and the nozzle diameter, the droplet size will vary. If the distance of the separate droplets is too large for merging, no closed layer will be formed. On the other hand, when droplets are too close, issues like overwetting or bulging may burden the feature size, which can be especially critical for thin lines. Therefore, the distance of neighboring droplets should be adopted accordingly by increasing the printing resolution to achieve first a wet film and after drying the designed pattern. The achievable resolution of inkjet printing is limited by the droplet size on the substrate and therefore greatly depends on the nozzle diameter and can reach values as low as ~20–30 μm. The printing speed for industrial applications can reach 3 m s^{-1} [47].

3.3.2. Aerosol jet printing

Another digital printing technique which has found considerable attention in printed electronics research is aerosol jet printing (figure 6(b)) [8, 48, 49]. As the name indicates, an ink aerosol is used, which is generated by ultra-sonication or by pneumatic atomization. This aerosol is transferred to the nozzle head by a carrier gas flow (typically nitrogen). In the nozzle head an additional gas flow is formed that coaxially sheathes the aerosol and helps controlling the diameter of the aerosol beam. Critical processing parameters include the atomization power, the gas flow rates, the nozzle diameter and in some cases the carrier gas temperature. Additionally, the printing speed is critical for the quality, thickness and linewidth of the printed patterns. As this technique is a single point deposition technique comparable to drawing with a pencil on paper, areas are constructed by consecutive printing of neighboring lines. Similarly, to inkjet printing, the distance between the lines has to be

adjusted to the single linewidth for a successful merging of the printed structure. The clear strengths of aerosol jet printing lie in the high resolution down to 10 μm feature size, wide range of possible ink viscosities (1–1000 cP), large bandwidth of printable materials (e.g. polymers, nanoparticles, -wires and -tubes) and facile deposition even on mm high 3D structures due to the relatively large nozzle to substrate distance of 5 mm.

4. Device engineering and fabrication of organic photodetectors

4.1. Device performance of printed and coated devices

In table 1 we summarize the performance parameters, materials and device architectures of OPDs processed partially or completely by printing and coating techniques which are reviewed in this report. An extended table containing additional information and references can be found in the supporting information is available online at stacks.iop.org/FPE/4/043001/mmedia. In the following sections we highlight the work which has contributed to the control and improvement of the device FOMs, namely $R(\lambda)$ and D^*, the dark current as well as the dynamic behavior. We also discuss the approaches in terms of materials, solvents and processing parameters which represent the state of the art in OPDs fabrication with industrial relevant techniques.

4.1.1. Spectral response range

The $R(\lambda)$ is the main criterion which qualifies an optical detector suitable for a specific application. It does not only define the operational wavelength range but also how much current is to be expected per incident optical power. For many basic applications of optical detectors, the wavelength range is not a critical parameter (e.g. for proximity sensors, ambient light sensors etc). Nevertheless, for specific applications certain windows of operation are of interest, such as the skin transmission band for pulse oximetry or the fluorescence of a given analyte in chemical detection.

The spectral range of an OPD is mainly defined by the optical absorption of the chosen active material which is given by the chemical structure of the compound. Figure 7(a) shows an overview of material systems employed in printed or coated OPDs with the achievable responsivity. $R(\lambda)$ is related to the actual photon-to-extracted carrier efficiency which also depends on device architecture characteristics such as the choice of interlayers, filters or device thickness. In the following, we will discuss both the material and architecture focused approaches employed for printed and coated OPDs.

To date, the most prominent material system utilized in OPDs is the BHJ comprised of Poly(3-hexylthiophene-2,5-diyl) and [6,6]-Phenyl C_{61} butyric acid methyl ester (P3HT:PC60BM). This material system exhibits an $R(\lambda)$ in the blue and green wavelength range up to a limit of ~600 nm defined by the band gap of P3HT. In 2009, Tedde *et al* were first to report the coating of P3HT:PCBM layers by spray and blade coating methods to fabricate OPDs with high performance [50]. The devices reached a $R(\lambda)$ of 300 and 330 mA W^{-1} at 550 nm. For the first reported printed active layer, inkjet printing was utilized, however, the performance was reported as low without further quantification of $R(\lambda)$ [84]. This work was followed by a detailed study of inkjet printed OPDs using P3HT:PCBM by Lilliu *et al* who were able to reach a comparable performance to coated devices with a $R(\lambda)$ of 280 mA W^{-1} [53].

The limited detection range of the P3HT:PCBM system ignited work on other approaches to broaden its spectral window. One method, consisted in the addition of a squarine dye to sensitize the $R(\lambda)$ of spray coated P3HT:PCBM BHJ devices extending its absorption towards the NIR regime [54]. While this approach reduced the magnitude in the region of the P3HT absorption, it reached ~160 mA W^{-1} at 800 nm enabling NIR imaging. Similarly, the use of a benzothiadiazole-based small molecule donor in combination with P3HT and the fullerene derivative [6,6]-Phenyl C_{71} butyric acid methyl ester (PC70BM) was investigated for inkjet printed ternary blend OPDs [57]. However, the device only reached values around 100 mA W^{-1} at 550 nm (green) and 80 mA W^{-1} at 650 nm (red).

Inspired by the success of alternative polymer donors in the OSC community, the OPDs community also moved towards replacements for P3HT. Lochner *et al* reported on the first blade coated active layer using a blend of Poly[[4,8-bis[(2-ethylhexyl)oxy]benzo[1,2-b:4,5-b']dithiophene-2,6-diyl][3-fluoro-2-[(2-ethylhexyl)carbonyl]thieno[3,4-b]thiophenediyl]] (PTB7) and PC70BM to achieve a broad band $R(\lambda)$ ranging almost over the entire visible spectrum up to 700 nm [11]. The device exhibited a maximum $R(\lambda)$ of 240 mA W^{-1} at 630 nm. The same active layer system has also been aerosol jet printed in a semitransparent device reaching 260 mA W^{-1} at 680 nm setting the record above the P3HT absorption regime at that time [8]. Recently, the use of a NIR absorbing polymer donor poly[(2,5-bis(2-hexyldecyl)-2,3,5,6-tetrahydro-3,6-diox-opyrrolo[3,4-c]pyrrole-1,4-diyl)-alt-([2,2':5',2''-terthiophene]-5,5''-diyl)] (PDPP3T) in a OPD with a spray coated active layer was reported [43]. PDPP3T enabled the extension of the spectral window up to 900 nm reaching a $R(\lambda)$ of 250 mA W^{-1} at this cut-off wavelength.

A very recent development in the OPD community is the use of novel high performance non-fullerene acceptors, which have the potential to replace the fullerene derivatives and offer increased stability, synthetic flexibility and most importantly for OPDs absorption tunability [85]. So far only two studies on

Table 1. Summary of reported figures of merit of printed or coated OPDs reviewed in this work. Additionally, the fabrication methods for the various layers is given. Values are taken directly from the referenced publication or calculated from the reported values if possible.

Substrate	OPD materials	Method	J_D (Bias) nA cm^{-2} (V)	$R(\lambda)$ (Bias) mA W^{-1} (V)	D^* 10^{12} Jones	LDR dB	$f_{3\ dB}$ (Bias) kHz (V)	Year	References
Glass/ITO	PEDOT:PSS/P3HT:PCBM/Ca/Ag	SC/BC/VE/VE	1000 (−5)	292 (−5)	0.13			2009	[50]
Glass/ITO	PEDOT:PSS/P3HT:PCBM/Ca/Ag	SpC/SpC/VE/VE	250 (−5)	305 (−5)	0.88		100[a]	2009	[50]
Glass/ITO	PEDOT:PSS/P3HT/PCBM/Al	IJ/IJ/SC/VE	1000 (−0.1)	250[a]				2009	[51]
Glass	Ag/PFB:F8BT/PEDOT:PSS	all IJ	1 (−1)	19 (0)				2011	[52]
Glass/ITO	PEDOT:PSS/P3HT:PCBM/Ca/Ag	IJ/IJ/VE	2000 (−5)	265 (−5)				2011	[53]
CMOS-chip	Al/P3HT:PCBM/PEDOT:PSS/PEDOT:PSS	VE/all SpC	7 (−1.5)	194 (−4)			15[a]	2012	[54]
CMOS-chip	Al/P3HT:SQ:PCBM/PEDOT:PSS/PEDOT:PSS	VE/all SpC	12 (−1.5)	151 (−4)				2012	[54]
PEN	Ag/PEIE/P3HT:PCBM/PEDOT:PSS	IJ/SC/IJ/IJ	200 (−1)	339 (−0.9)	1.5		20 (−1)	2013	[6]
PMMA-Fiber	PEDOT:PSS/P3HT:PCBM/Al	SpC/SpC/VE	10 (−1)	10.6 (−1)			15[a]	2013	[55]
Glass/ITO	PEIE/PBDTTT-C:PC70BM/PEDOT:PSS/Ag	SC/SC/IJ/IJ	2 (−2)	165 (−2)	8	140	12[a]	2013	[56]
PEN	Ag/PFN/T1:P3HT:PC70BM/PEDOT:PSS	IJ/SC/IJ/IJ	100 (−1)	113 (−1)				2014	[57]
PEN	PEDOT:PSS/PFN/T1:P3HT:PCBM/PEDOT:PSS	IJ/SC/IJ/IJ	1000 (−1)	152 (−1)				2014	[57]
PEN	PEDOT:PSS/PEDOT:PSS/PTB7:PC70BM/Al	all BC/VE	1 (−1)	254 (0)			10 (0)	2014	[11]
PEN	Au/P3HT:PCBM/Al	VE/IJ/VE	25 (−1)					2014	[58]
PET	CNT/PEDOT:PSS/P3HT:PCBM/LiF/Al	all SpC/VE/VE	500 (−5)	315 (−5)				2014	[59]
Paper	Ag/P3HT:PCBM/DNA-polymer/PEDOT:PSS	IJ/IJ/DC/IJ	9375 (−1)	2 (−1.5)			0.1 (−1.5)	2014	[60]
Glass	PEDOT:PSS/PEDOT:PSS/P3HT:PCBM/Al	all SpC/VE	100 (−1)	242 (−4)			1[a]	2014	[61]
PET/ITO	AZO/PTB7:PC70BM/PEDOT:PSS	all AJ	21.9 (−1)	250 (−3)	2.2[b]		330 (−3)	2015	[8]
PET	PEDOT:PSS/AZO/PTB7:PC70BM/PEDOT:PSS	all AJ	2200 (−1)	260 (−3)	0.27[b]		300 (−3)	2015	[8]
PEN	PEDOT:PSS/PEIE/PCDTBT:PC70BM/PEDOT:PSS	all BC/SP	0.35 (−3.33)	296 (−3.3)	28[b]		50 (−5)	2015	[62]
Glass/ITO	PEI/P3HT:PCBM/PEDOT:PSS/PEDOT:PSS	all SpC	<100 (−4)	315 (−4)			15[a]	2015	[63]
Glass	PEDOT:PSS/PEI/P3HT:PCBM/PEDOT:PSS/PEDOT:PSS	all SpC	<100 (−4)	288 (−4)			6[a]	2015	[63]
a-Si/ITO	TFB/P3HT/P3HT:PCBM:GOS:Tb/Al	SC/SpC/SpC/VE	10 (−2)					2015	[64]
PET	EG:PEDOT:PSS/PEDOT:PSS/P3HT:PCBM/Al	SpC/SC/SC/VE		160 (0)	1.33[b]			2015	[65]
PET	Ag/AZO/PTB7:PC70BM/PEDOT:PSS	brush/all AJ	100 (−1)	<300 (−1)				2016	[66]
PEN	PEDOT:PSS/PEI/P3HT:PCBM/Poly-PT/PEDOT:PSS	IJ/SC/all IJ	75.8 (−1)	288 (−1)	2.2[b]			2016	[67]
Glass/ITO	PEIE/PCDTBT:PCBM/PEDOT:PSS	SC/SC/SP	0.3 (−2)	320 (−2)	32.1[b]	148	91 (−2)	2016	[2]
Glass/ITO	P3HT:PCBM/LiF/Al	TP/VE/VE	53 (−1)	262 (−5)				2016	[68]
Ormostamp	Al/PEDOT:PSS/P3HT:PCBM/LiF/Al	VE/SpC/SpC/VE/VE	800 (−5)	194[a]				2016	[69]
Glass	Al/PEIE/P3HT:PCBM/(MoO3/Ag/MoO3)	VE/SpC/TP/VE	994 (−1.5)	75 (−1.5)	0.14[b]			2017	[70]
PEN	Ag/PEI/P3HT:PCBM/PEDOT:PSS/PEDOT:PSS	IJ/all SpC	200 (−2)	339 (−4)				2017	[71]
PEN	Al/P3HT:PCBM/PEDOT:PSS/PEDOT:PSS	VE/all SpC	100 (−5)					2017	[72]
Glass/ITO	PEIE/PCBM/P3HT/MoO3/Ag	SC/SC/TP/VE/VE	7.72 (−1.5)	240 (−1.5)				2017	[73]
Glass/ITO	ZnO/P3HT:PCBM/PEDOT:PSS	SC//SC/IJ		110[a]				2017	[74]

Table 1. (Continued.)

Substrate	OPD materials	Method	J_D (Bias) nA cm^{-2} (V)	$R(\lambda)$ (Bias) mA W^{-1} (V)	D^* 10^{12} Jones	LDR dB	$f_{3\ dB}$ (Bias) kHz (V)	Year	References
Glass	Ag/ZnO/PTB7:PC70BM/PEDOT:PSS	IJ/all AJ	90 (−0.5)	300 (−1)	2[b]	114	100 (0)	2018	[8]
Glass/ITO	ZnO/P3HT:IDTBR/PEDOT:PSS	IJ/IJ/AJ	3000 (−1)	170 (−2)	0.002		250 (−2)	2018	[35]
Glass/ITO	ZnO/P3HT:IDTBR/PEDOT:PSS/Ag	IJ/IJ/SC/VE	10 000 (−1)	280 (−2)	0.152		2000 (−2)	2018	[35]
PEN	PEDOT:PSS/PEI/P3HT:PCBM/PEDOT:PSS	all IJ	57 (−1)	195 (−1)	3.3[b]			2018	[75]
a-Si/ITO	ZnO/P3HT:IDTBR/MoO3/Al	SC/SpC/VE/VE	21 (−5)	380 (−5)	4.57[b]		12.4 (−5)	2018	[15]
a-Si/ITO	ZnO/P3HT:IDTBR/MoO3/Al	SC/BC/VE/VE	34 (−5)	420 (−5)	3.98[b]		52.6 (−5)	2018	[15]
IGZO-TFT	electrode/poylmer:PCBM/electrode	−/BC/-	0.1 (−2)	190[a]	80[b]			2018	[9]
PEN	PEDOT:PSS/PEIE/PV-D4650:PC70BM/PEDOT:PSS	all BC/SP	0.5 (−5)	236 (−4)		100	1.1 (−5)	2018	[76]
Glass/ITO	PEDOT:PSS/PTB7:PCBM/Al	SC/TP/VE	7630 (−1)	410 (−1)	0.263[b]			2018	[77]
Glass/ITO	TFB/PDPP3T:PC70BM	SC/SpC/VE	20 (−5)	254 (−5)	3.34[b]	60	63.8 (−5)	2018	[43]
Glass/ITO	TiOx/P3HT:PCBM/MoO3/Ag	IJ/IJ/VE/VE	27 000 (−2)	161 (−2)				2018	[78]
Glass/ITO	PEDOT:PSS/P3HT:PCBM/Al	SpC/SpC/VE	29 (−1)					2018	[79]
PEN	PEDOT:PSS/CDT Donor:PC70BM/Al	BC/BC/VE	10 (−0.5)	226[a]		60	5[a]	2018	[80]
Glass/ITO	TFB/PV-D4650:PCBM/Al	SC/SpC/VE	0.034 (−5)	440 (−5)	21.9	160	50 (−5)	2019	[81]
Glass/ITO	PEDOT:PSS/PVK:PCBM/PFN/Poly-TPD/PVK:PCBM/Bphen/Ag	SC/SC/SpC/SC	7 (−1.5)		0.13[b]			2019	[82]

Note. SC = spin coating, VE = vacuum evaporation, BC = blade coating, SpC = spray coating.
SP = screen printing, TP = transfer printing, IJ = inkjet, AJ = aerosol jet.

[a] No bias voltage specified.

[b] Specific detectivity calculated from dark current with shot noise approximation.

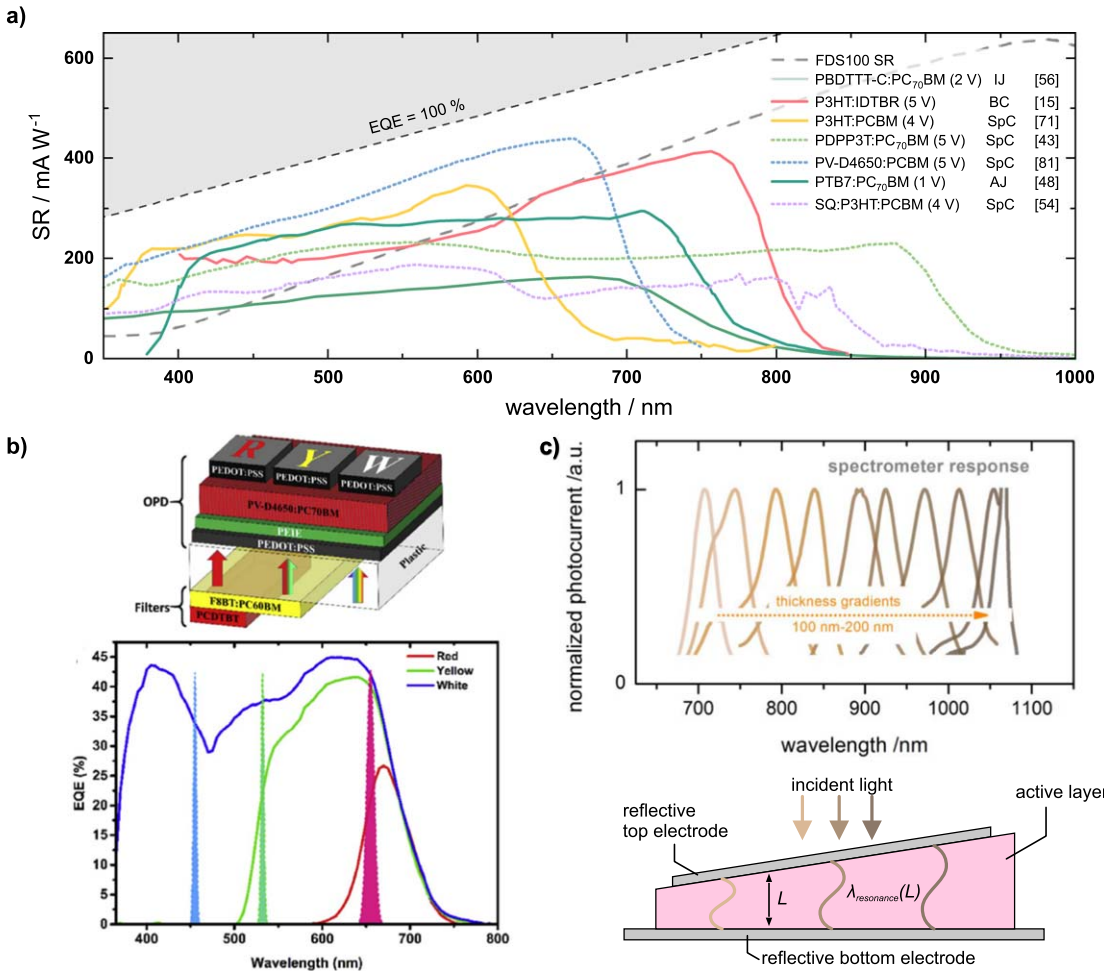

Figure 7. (a) Overview of material systems in the active layer and corresponding $R(\lambda)$ of OPDs partially or fully fabricated with coating and printing techniques (IJ: inkjet, AJ: aerosol jet, BC: blade coating, SpC: Spray coating). The $R(\lambda)$ from a commercial Si-photodiode (FDS100) is shown as a reference curve. (b) Cross section (top) and EQE at −4 V of color selective coated OPDs through color filters. The resulting 'white', 'yellow' and 'red' OPDs at −4 V bias were capable of reconstructing the intensity contributions of RGB-LEDs that have the displayed emission spectra. Reprinted with permission from [76], (CC-BY 2018) (c) Cavity enhancement of charge-transfer absorption allows for narrow NIR response depending on the thickness L of the active layer which defines the resonance wavelength $\lambda(L)$. The spectrum is reprinted with permission from [83], Copyright (2017) John Wiley and Sons.

printed/coated devices have been published, both of them using P3HT in combination with the NFA IDTBR which has a chemical structure consisting of an indacenodithiophene core with benzothiadiazol and rhodanine flanking groups. The absorption of IDTBR up to 750 nm complements the P3HT absorption and enables the fabrication of broad band OPDs. Gasparini *et al* utilized the blade and spray coating technique with evaporated MoOx-Al top contacts [15], while Strobel *et al* developed a process for fully printed devices utilizing inkjet and aersol jet [35]. Both reports were able to set record responsivities for their fabrication technique by achieving $R(\lambda)$ around 400 and 300 mA W^{-1} at 750 nm, respectively.

Beside the extension of $R(\lambda)$ towards the NIR there are also applications for OPDs that demand a selective or even narrow band response of the device. The most prominent example is represented by the application of OPDs in image sensors where separate pixels should only be sensitive to certain spectral regions (e.g. colors such as red green and blue). For inorganic imagers this is realized by applying optical filters on broad band absorbing Si-photodiodes to limit their spectral response. Deckman *et al* followed this filtering approach to fabricate wavelength selective OPDs as shown in figure 7(b). For this purpose, two different organic filter layers were spray coated on the opposite side of the substrate where a broad band (Lisicon PV-D4650:PC70BM) OPD array was fabricated by a combination of printing and coating methods. The optical filters were composed of a blend of Poly(9,9-di-n-octylfluorene-alt-benzothiadiazole) (F8BT) and PCBM (10:1) for the yellow band and a bilayers of this blend with the polymer Poly[N-9′-heptadecanyl-2,7-carbazole-alt-5,5-(4′,7′-di-2-thienyl-2′,1′,3′-benzothiadiazole)] (PCDTBT) for red transmission. The resulting OPD array exhibited three different spectral responses (red, yellow and white) which enabled the reconstruction of the color composition (i.e. wavelength ratios) of the incident light [76].

Another approach to achieve a selective response was achieved by utilizing cavity enhanced charge-

transfer state absorption to fabricate narrow band photodiodes with a full-width-half-maximum down to 14 nm [83]. For this purpose a poly(2,5-bis(3-tetradecylthiophen-2-yl)thieno[3,2-b]thiophene) (PBTTT):PCBM active layer, which usually shows a broadband absorption below 600 nm, was sandwiched between two reflective electrodes to form an optical cavity (see figure 7(c)). This resulted in a narrow resonance whose wavelength depends on the thickness of the active layer. By fabricating an OPD with an active layer thickness gradient through blade coating, a spectrometer was realized, which was capable of measuring the transmittance spectrum of water.

Both approaches, using optical filters and exploiting optical effects, are successful in achieving a wavelength selective response, however, they burden device fabrication by requiring additional processing steps or relying on a very accurate control over the layer thicknesses. A much simpler approach is the use of intrinsic absorption of materials with narrow absorbing bands. So far, there is little research in this direction as it diverges from the requirements of broad band absorption given by OSC optimized materials. Yang *et al* and Nakamichi *et al* have reported the fabrication of printed narrow band OPDs by following this material-based approach [86–88]. They demonstrate the use of inkjet printed active layers containing Poly(3,4-ethylenedioxythiophene)-poly(styrenesulfonate) (PEDOT:PSS) and cyanine dyes to fabricate a detector capable of resolving a laser wavelength shift of ~1 nm.

We believe that future work on printed OPDs will be evolving increasingly around the development of wavelength selective devices for example by employing the approach to use thick active layers which selectively attenuate a part of the incident light spectrum [24].

4.1.2. Specific detectivity and dark current

While $R(\lambda)$ represents the light-to-current wavelength profile of an OPD, it does not consider the lowest detection limit. This lowest threshold is restricted by the noise of the photodetector, which is quantified by D^* as a parameter to compare among different detectors. As explained in section 2.4 one of the strongest contributions to the noise stems from the magnitude of shot noise which is directly linked to the dark current. Therefore, many studies have been devoted to its analysis and reduction in OPDs. Two main approaches can be distinguished in this regard, the fabrication of thick active layers and the use of charge blocking and work function modifying interlayers (see figure 8(a)). In the following, we discuss its utilization in OPDs fabricated through printing and coating techniques.

In their pioneer work, Tedde *et al* were the first to report on dark currents in OPDs with coated active layers [50]. Specifically they analyzed the dependence of dark current on the active layer thickness, roughness and fabrication technique. It was found that spray coated layers of ~450 nm thickness showed the lowest dark current of 250 nA cm^{-2} compared to blade coated (250 nm, 500 nA cm^{-2}) at a reverse bias of 5 V. Surprisingly, this was achieved although the sprayed layer had a much higher surface roughness. It was argued that the layer thickness is capable to overcome drawbacks stemming from the roughness. The same conclusion was drawn by Schmidt *et al* who found a decrease in dark current for increasing active layer thickness for spray coated P3HT:PCBM active layers as shown in figure 8(b) [61]. This also holds true for avoiding shunts due to the roughness of the underlying layer as reported by Falco *et al* who spray coated thick active layers on a carbon nanotube electrode achieving their best results for layers >650 nm [59].

However, the increase of the active layer thickness has drawbacks in terms of a reduced detection speed as carrier transit time increases. This has strongly motivated the research on interlayers to block unwanted charge injection. A large number of works have studied and confirmed the benefit of materials like poly (ethylenimine) (PEI), poly(ethylenimine) ethoxylated (PEIE) or Poly [(9,9-bis(3'-(N,N-dimethylamino)propyl)-2,7-fluorene)-alt-2,7-(9,9–dioctylfluorene)] (PFN) as suitable hole blocking layers to successfully repress dark current in printed devices [2, 6, 56, 57]. However, the requirement of having an ultrathin and pinhole free layer forced all of these early reports to employ spin coating as deposition technique. Falco *et al* were the first to successfully spray coat a closed and sufficiently thin layer of PEI [63]. By a variation of the spraying time and the ink concentration between 5 and 20 s and 0.05 and 0.4 wt% they were able to tune the thickness, roughness and work function of the PEI layer. For 0.1 wt% and 10–15 nm thickness an optimal device performance with dark currents below 100 nA cm^{-2} and EQEs above 60% at −4 V reverse bias was found (see figure 8(c)). Their developed process further enabled them to fabricated the first fully spray coated OPDs on conductive PEDOT:PSS electrodes with similar device performance. Their work was followed by the development of a blade-coating process for a thin PEIE layer on PEDOT:PSS [62]. Through a combination of coating and printing they fabricated devices with record dark currents <1 nA cm^{-2} and detectivities above 10^{13} Jones. Furthermore, they highlight that the interlayer approach has a much larger effect on the reduction of the dark current compared to increasing the BHJ thickness. The first printed demonstration of PEI in OPDs was reported recently by Cesarini *et al* [75] They employed inkjet printing to deposit PEI on PEDOT:PSS for fully inkjet printed OPDs and investigated the reproducibility of the device performance in a very comprehensive manner obtaining dark currents on the order of 60 nA cm^{-2} at −1 V and specific detectivities $>10^{12}$ Jones. In addition to the wide selection of hole blocking layers, the electron blocking capability should also be considered. Recently, Grimoldi *et al* investigated poly[3-

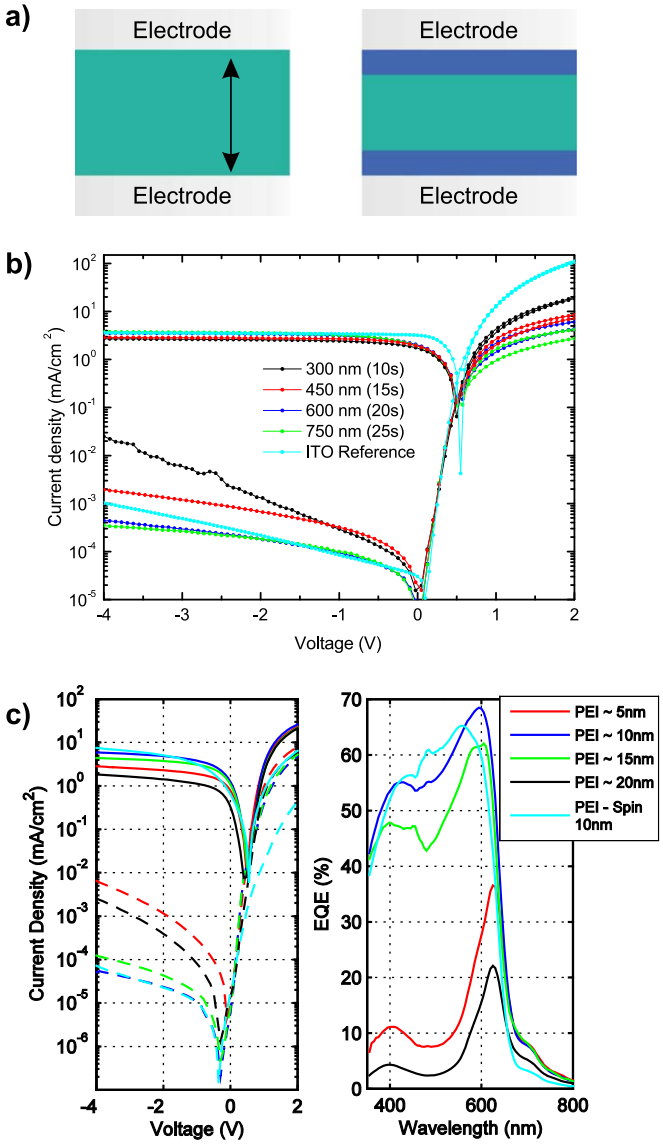

Figure 8. (a) Schematic of the two approaches to lower the dark current in OPDs: thicker active layers (left) and the introduction of interlayers for charge blocking or work function modification (right). (b) Dark and light *IV*-curves for spray coated P3HT:PCBM active layers of different thickness. The thickness is controlled by the spraying time and improves the dark current up to a saturation point of ~300 nA cm^{-2} at −4 V. Reprinted with permission from [61], (CC-BY 2014) (c) *IV*-curves and EQEs of spray coated P3HT:PCBM OPDs with varying thickness of a PEI interlayer. An optimal thickness of 10 nm showed low dark currents of <100 nA cm^{-2} and EQEs >60%. Reprinted with permission from [63] Copyright © 2015 Elsevier B.V. All rights reserved.

(3,5-di-tert-butyl-4-methoxyphenyl)-thiophene] (poly-PT) as an alternative. The inkjet printed interlayer showed a two-fold improvement regarding the dark current reaching 75 nA cm^{-2} at −1 V and a considerable benefit in terms of processability which will be discussed in section 4.2.2 [67].

Besides these two approaches, a third idea exploiting a segregated BHJ morphology was investigated by Abdellah *et al* and Kim *et al* Both groups utilized transfer printing to fabricate a P3HT/PCBM bilayer. By a subsequent thermal post treatment, material inter-diffusion should allow for a controlled BHJ morphology enabling efficient charge separation and transport without the drawback of having an interfacial contact between the respective electrodes and the donor or acceptor material. This should strongly limit the injection of charges under reverse bias. Both groups found the thermal treatment to improve devices performance under illumination as expected, almost reaching the performance of reference devices with a blended BHJ. Nevertheless, dark currents were not observed to improve compared to the reference device [68, 73].

The successful reduction of dark current and thus noise in OPDs will also improve the LDR as the noise floor limits the detectable signal in the low intensity regime. Record LDR values correlate with record dark currents and are currently on the order of 150–160 dB (see table 1) [2, 81]. Unfortunately, the LDR is often not reported in literature and in some cases evaluated wrongly from a non-unity slope dependence indicating nonlinear $R(\lambda)$. Furthermore, the high intensity

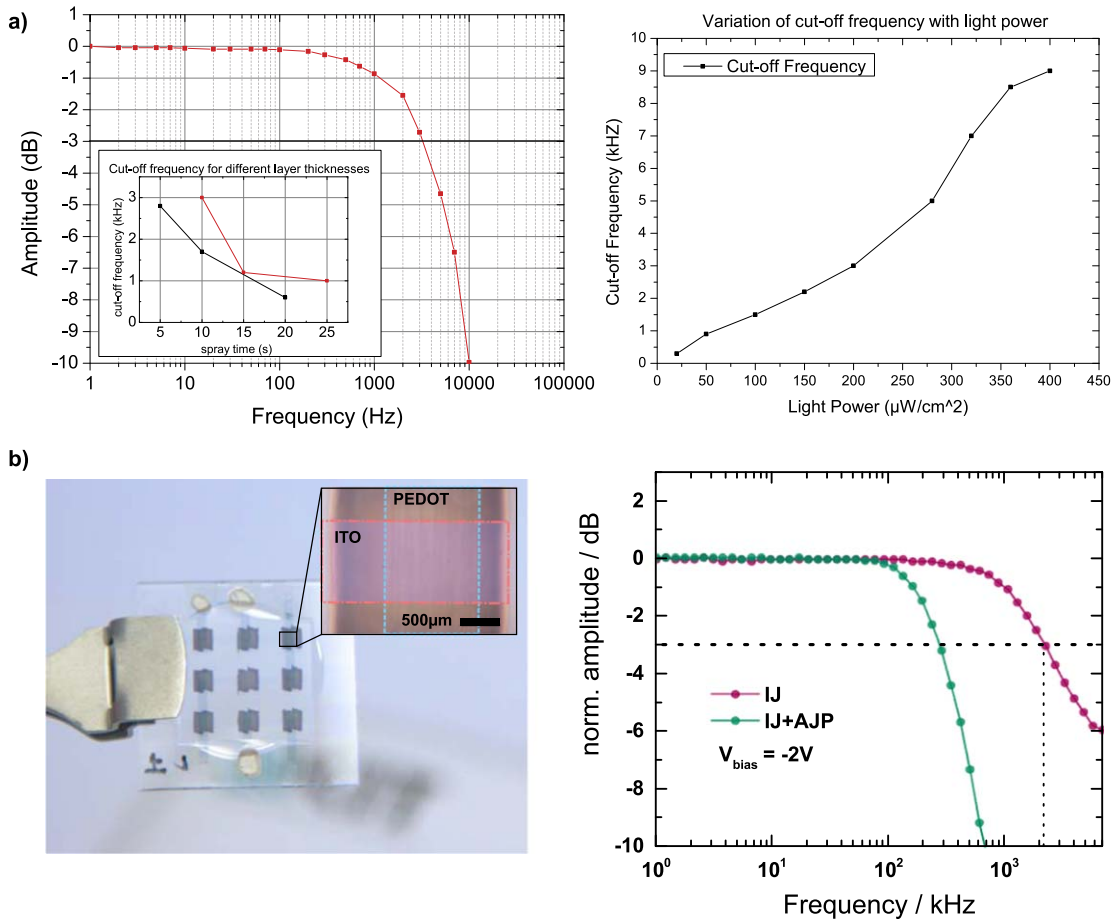

Figure 9. (a) Detection speed of a spray coated P3HT:PCBM active layer OPD (left) and the dependence on different active layer thicknesses (inset) as well as on the light intensity (right). Reprinted with permission from [61] (CC-BY 2014). (b) Photograph and microscopy image of digitally printed P3HT:IDTBR OPDs (left) as well as the recorded detection speed depending on the top electrode material (IJ: silver; AJ: PEDOT). Reprinted with permission from [35], Copyright 2018 American Chemical Society.

saturation is rarely regarded in detail leaving room for future analysis and potential improvement of the LDR in next generation OPDs.

4.1.3. Detection speed and bandwidth

The tremendous developments in the field of printed OPDs in recent years have demonstrated that the fabricated devices have reached a competitive performance to that of lab scale organic and commercial inorganic technologies. However, this comparison is mostly valid for the steady state performance. The dynamic performance of printed OPDs is generally lagging behind in performance for most material systems. This can in part be attributed to the relatively low charge carrier mobilities of organic materials compared to their inorganic counterparts. On the other hand, only recently some effort has been placed on the improvement of device speed as most reports characterizing cut-off frequencies or response times merely discuss the possible reasons limiting the dynamic response rather than addressing the underlying problems.

The first transient measurements in partially inkjet printed devices were reported and discussed by Azzelino *et al* [6]. They investigated the dependence of the photocurrent fall time and found a correlation to the illumination intensity, where the devices exhibited response times between 100 ms and 90 μs at intensities of 20 and 1000 μW cm^{-2}, respectively. The photocurrent fall time was defined as the time needed for a reduction from 90% to 10% of the dc-signal after the optical excitation had stopped. This dynamic behavior was attributed to a transit limited regime dominated by trapping and detrapping effects. Similar effects have been observed by others like Schmidt *et al* in spray-coated devices with evaporated Al cathodes as depicted in figure 9(a). Furthermore, they demonstrated the influence of the spraying time and the resulting BHJ thickness on the device speed, as it increases the transit time of charge carriers and thus reduced the cutoff frequency from 3 to 1 kHz [61]. An optimal active layer morphology is critical in that regard. Benavides *et al* were able to increase the cut-off frequency of their devices with spray coated active layers from 738 Hz to 63.8 kHz by using 1,8-diiodooctane (DIO) as an additive [43]. Other investigated approaches in literature like the addition of insulating polymers to decrease trapping and increase device speed could result

beneficial for the device performance of printed devices in the future [89]. Aside from the active layer, also interlayers play a crucial role in the response speed. Grimoldi *et al* found a slightly reduced performance in terms of response time, which reached 106 μs without and more than 136 μs with poly-PT as an electron blocking layer (EBL) and hypothesized that additional hole traps in the interlayer or at the interface might be the reason [67]. Furthermore, the commonly used PEI has been shown to have a detrimental effect on the detection speed when the layer is of low quality [75]. Especially the water-based ink utilized in this study seems to induce losses in performance.

When a device operates outside the transit limited regime, it is generally constrained by the *RC*-constant of the device. This limit is determined by the overall device resistance and geometric capacitance. Therefore, the choice of electrode material or device dimensions has a great impact on the device dynamic characteristics. Several studies have shown that the use of PEDOT:PSS as a replacement for ITO or a metal electrode will strongly limit the cut-off frequency due to the increased electrode resistivity [2, 8, 35, 63]. In order to improve the detection speed one has to carefully consider the different parameters limiting the response. In the work by Strobel *et al* the device geometry was adjusted with the transit and *RC* trade-off in mind. An active layer thickness of 200 nm was found to represent a good balance between both limits, which enabled record detection speeds above 2 MHz for inkjet printed devices with ITO and silver electrodes [35]. The replacement of the metal electrode by PEDOT:PSS produced the afore mentioned increase of the series resistance and the resulting drop in device speed (see figure 9(b)). Further speed improvement therefore could be enabled by the use of high conductive electrodes like carbon nanotubes (CNTs) or Silver nanowires.

4.2. Process engineering and performance

In order to realize high-performance OPDs by printing or coating techniques, it is necessary to consider the requirements and functionality of every single layer of the device. Furthermore, the ink formulation and processing parameters have to be adopted according to the constraints of the chosen fabrication technique. Most of the times, a combination of fabrication techniques and chemical approaches (i.e. crosslinking, orthogonal solvents, etc) is necessary to realize an optimized device architecture. The following section discusses the currently developed device processing approaches which enable or facilitate printability and optimal device performance.

4.2.1. Active layer ink formulation and processing techniques

The active layer of an OPD defines the functionality and application field of the device while interlayers are usually employed to improve performance. It is therefore logical that it was the first layer of an OPD which was fabricated by printing or coating with the goal of obtaining reproducible and homogeneous layers. First reports on printed or coated active layer devices employed the same ink systems that have previously been used for spin coated devices relying on single solvent systems like xylene, chlorobenzene (CB) or dichlorobenzene (DCB). These reports demonstrated that these simple inks are sufficient to obtain working active layers by blade coating [11, 50, 62, 76] or spray coating techniques with state of the art $R(\lambda)$ [11, 50, 59, 61, 62, 76, 79]. Especially for blade coated layers drying effects where not reported to be an issue and the layer roughness was in the range of tenths of nm. For spray coating on the other hand, the layers were typically of high roughness in the range hundreds of nm. However, the drawbacks of this roughness, like the risk of shunts, were often overcome by fabricating very thick layers by simply increasing the spraying time. However, the thick active layers also lead to an increase in charge transit times and therefore to higher recombination and reduced device speed [61]. A possibility to reduce the roughness was demonstrated by Benavides *et al* through the use of the additive diiodooctane (DIO), which is often used in literature to improve the BHJ morphology for various polymer: fullerene active blends. In their study they showed that DIO additionally reduced the surface roughness of a spray coated layer of PDPP3T:PC70BM from a peak-to-peak roughness of 600 nm down to 200 nm as shown in figure 10(a) [43]. Consequently, device performance parameters improved, including dark current, responsivity and dynamic response. This effect was attributed to the combination of a slower drying rate and smaller droplets from the lower viscosity of the ink and has also been employed in other BHJ systems [81].

Very low layer rms roughness on the order of 6 nm on PTB7:PC70BM BHJ OPDs was reported by Eckstein *et al* who used aerosol jet printing as a fabrication tool [8]. Although this technique is also a droplet based process similar to spray coating, the consecutive line by line deposition and the smaller droplet size benefit the formation of smooth layers. However, it was further reported that the roughness strongly depends on the printing parameters leading to a 10 fold increase when the atomizer flow rate is reduced from 16 ccm to 13 ccm (see figure 10(b)).

The most prominent printing technique for the fabrication of active layers is inkjet printing as is clearly shown in figure 3. The first report of its use for OPDs was published by Lavery *et al* in 2011 [52]. Notably, it was also the first fully printed OPD. In this study the active layer blend was composed of poly(9,9′-dioctylfluorene-co-bis-N,N′-(4-butylphenyl)-bis-N,N′-phenyl-1,4-phenylene-diamine) (PFB) and poly(9,9′-dioctylfluorene-co-benzothiadiazole) (F8BT). It was printed from a single solvent DCB solution on top of a

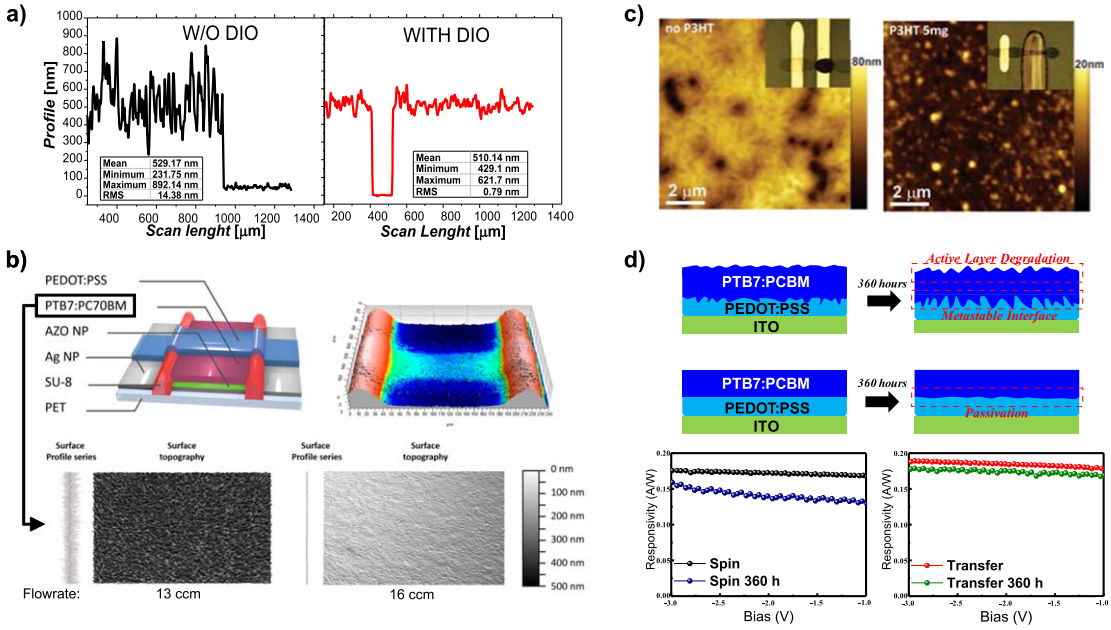

Figure 10. (a) Surface profile of spray coated PDPP3T:PC70BM active layers with and without DIO as an additive. Reprinted with permission from [43], ©2017 Elsevier B.V. All rights reserved. (b) Schematic layout and white light interferometry image of an aerosol jet printed OPD (top) as well as the surface topography PTB7:PC70BM active layers with different atomizer flow rates (bottom). Adapted with permission from [23], (CC-BY 2016) (c) Atomic force microscopy images of inkjet printed T1:PCBM binary and P3HT: T1:PCBM ternary active blends for OPDs. The insets show the dewetting issues and nice printability of the two blends, respectively. Reprinted with permission from [57], ©2014 WILEY-VCH Verlag GmbH & Co. KGaA, Weinheim. (d) Schematic description of the stability benefit of transfer printed PTB7:PC70BM active layers on PEDOT interlayers (lower diagram) and the resulting improved lifetime of OPDs regarding spectral responsivity compared to spin coated devices (upper diagram). Reprinted with permission from [77], Copyright 2018 American Chemical Society.

silver bottom electrode. However, it was found relatively quickly that the quality of layers fabricated by inkjet printing is much more sensitive to the solvent system used. Single solvent systems typically result in homogeneity issues and material displacement due to drying effects (e.g. coffee ring) [84]. It has been shown that these issues can be overcome to some extent by varying the concentration of the ink to increase the viscosity [90], or by adapting the substrate temperature to prevent or enable spreading of the ink during drying in systems comprising of P3HT:PCBM [78]. However, the more widely used approach is represented by the use of multi-solvent systems to balance the evaporation rates and dynamic surface tension effects during drying which at the same time allows control of the ink viscosity. In many studies with the prominent P3HT:PCBM BHJ system, a solvent mixture of DCB and mesitylene in the ratio 68:32 has proven to be very beneficial to achieve high quality layers. It has first been suggested in a report on printed OSCs [91]. Later on, Lilliu *et al* were the first to make use of this ink system for printed OPDs [53], followed by the study of Azzelino *et al* who further adapted the concentration of the semiconductors to avoid an unwanted coffee-ring during drying and found a blend concentration of 30 mg ml^{-1} to yield the highest performance [6]. However, this solvent mixture cannot be universally applied as is demonstrated by Pace *et al* in their investigation of a small-molecule BHJ system, where coffee-ring formation could only be alleviated by the addition of P3HT to form a ternary BHJ [57]. The added polymer helped to control the viscosity and reduced the material displacement after deposition allowing for printed active layers displayed in figure 10(c). They further referred to the addition of insulating polymers to reach a similar effect as has been done by others in literature [89, 92, 93]. Another solvent mixture was investigated by Strobel *et al* in their work with P3HT and the NFA IDTBR [35]. They inkjet printed the active layer from a solution of CB adding 5 vol% of the high-boiling point solvent tetralene to overcome the coffee-ring effect.

A common issue presented in the fabrication of any solution processed multilayer device is the dissolution of the underlying layers. This is typically addressed by the use of an orthogonal solvent approach. Another alternative was presented by Abdellah *et al* and Kim *et al* who use the transfer printing technique, allowing the deposition of a layer without affecting the previous one. They fabricated bilayers of P3HT and PCBM, demonstrating that a comparable performance (~280 A W^{-1}) to a BHJ can be reached through post thermal treatment after the stamping step [68, 73]. This technique was further used to fabricate OPDs on a three-dimensional semispherical surface by developing a 3D-PDMS stamp to deposit the P3HT:PCBM active layer. Additionally, it is possible to replace the polydimethylsiloxane (PDMS) stamp, which is typically used for this technique, by chemically modified polyurethane acrylate (PUA) [77]. This

allows for a fine tuning of the surface energy and provides higher chemical and temperature resistance. OPDs comprising of PTB7:PC70BM as active layer were fabricated with such a PUA. The devices showed improved photocurrent and interestingly improved stability over the time span of 360 h. This was attributed to a stabilized dry layer formation prior to stamping, which prevents penetration of the BHJ layer into the PEDOT:PSS blocking layer as depicted in figure 10(d).

4.2.2. Design of printable device architectures

While the active layer fabrication is mainly focused on the control of blend morphology and the prevention of inhomogeneities caused during drying, the complexity in printed devices (and generally in thin film electronics) rises tremendously due to the challenge to obtain interfaces of high optoelectronic quality when printing interlayers and electrodes. The former typically demand for ultra-thin (<10 nm) but closed layers for combined efficient carrier blocking and extraction. The latter needs to fit the device energetic requirements and exhibiting high conductivity, furthermore at least one electrode has to be transparent in the optical region of interest. Additionally, in terms of processing the surface free energy of all layers needs to be optimized and degradation of the underlying layers must be prevented. In order to tackle this complex web of constraints, the OPD stack design and the material-property relations of the device components should be carefully considered from the conceptualization stage of the photodetector.

The first reports on OPDs with printed/coated interlayers or electrodes were fabricated in the so-called standard device architecture with the EBL on the bottom and the cathode on the top of the device. In this configuration, the top electrode has been typically thermally evaporated due to the lack of suitable materials with a low work-function (WF) which are solution-processable. The most prominent interlayer for EBLs is PEDOT:PSS. For OPDs, the translation of PEDOT:PSS fabrication by spin coating to a scalable technique was the focus of the first investigations by spray coating, blade coating and inkjet printing [50, 53]. These reports showed that all techniques enabled continuous layers with a thickness on the order of 200 nm on top of ITO. Similarly as for the active layers, Spray coating of PEDOT:PSS yielded layers of much higher roughness than blade coating with an rms value of 33 nm and 14 nm, respectively [50]. However, both processes still achieved smoother films than the inkjet printed layer, which were as rough as 97 nm [53]. Multiple printing steps with a successive substrate rotation of 90° were necessary to achieve continuous films of reasonable roughness. The poor compatibility of water-based solutions with low boiling point and high surface tension can be identified as the underlying issue.

Following this investigation, others have considered alternatives to replace the ITO electrode by a solution processable material. The most straight forward replacement of ITO is represented by the use of high conductive PEDOT:PSS. This has first been utilized by Schmidt *et al* who sprayed PEDOT:PSS (Clevios PH1000) on float glass [61]. Sufficient wettability was achieved by addition of the wetting agent Dynol 604. For the fabrication of their OPDs an additional layer of PEDOT:PSS (Clevios PVP CH 800) was sprayed as a EBL on top of the electrode in order to improve the blocking capabilities. The PH 1000 electrode can further be modified by addition of exfoliated graphene (EG). Liu *et al* spray coated such a mixture of EG and PH1000 on flexible polyethylene terephthalate (PET) substrates to fabricate OPDs [65]. They reach conductivities in the range of 1000 S cm^{-1} for films with a thickness of only 20 nm. They highlight the high mechanical flexibility of the electrode and demonstrate ultra-thin and stretchable OPDs on PET foils as thin as 2.5 μm (see figure 11(a)). In 2014 Falco *et al* investigated the use of CNTs as an electrode for OPDs. They successfully spray coated electrodes through a shadow mask on glass and PET substrates with a sheet resistance of 160 Ωsq^{-1} [59]. However, the resulting hydrophobic surface of the CNT electrodes represented a problem for the successive deposition of the water-based PEDOT:PSS dispersion. A mild oxygen plasma treatment was found to improve the wettability and reduce the water contact angle from 50° to 16°. However, this resulted in a slight decrease of performance due to an increase in the resistance of the CNT electrode. A more successful approach was the addition of isopropanol to the PEDOT:PSS ink formulation. This resulted in a contact angle of 24° and considerably improved the performance of the OPDs as well as the fabrication yield.

For inverted architectures PEDOT:PSS has been one of the main candidates as transparent top electrode. However, the processability of this water-based dispersion on top of the active layer is not trivial. While screen printing of PEDOT:PSS from a very high viscosity ink (80% Agfa EL-P5015 with >50 Pa s) has yielded working OPDs [62], other techniques requiring lower viscosity (e.g. inkjet printing) often face problems of dewetting due to the low surface free energy of most active materials. A common approach, is the use of a surfactant like Zonyl FS-300, as an additive for the PEDOT:PSS ink in weight ratios up to 10% [6, 8, 52, 57, 75]. Zonyl is a water-soluble fluorinated surfactant which helps to reduce contact angle and prevent dewetting.

Aside from the use of additives in the ink formulation, it is also possible to modify the surface of the active layer in order to obtain improved wetting of the ink on the substrate. Plasma treatment is a very common and effective way to increase the surface energy by introduction of polar groups on substrates such as glass or ITO and it has been used to improve the

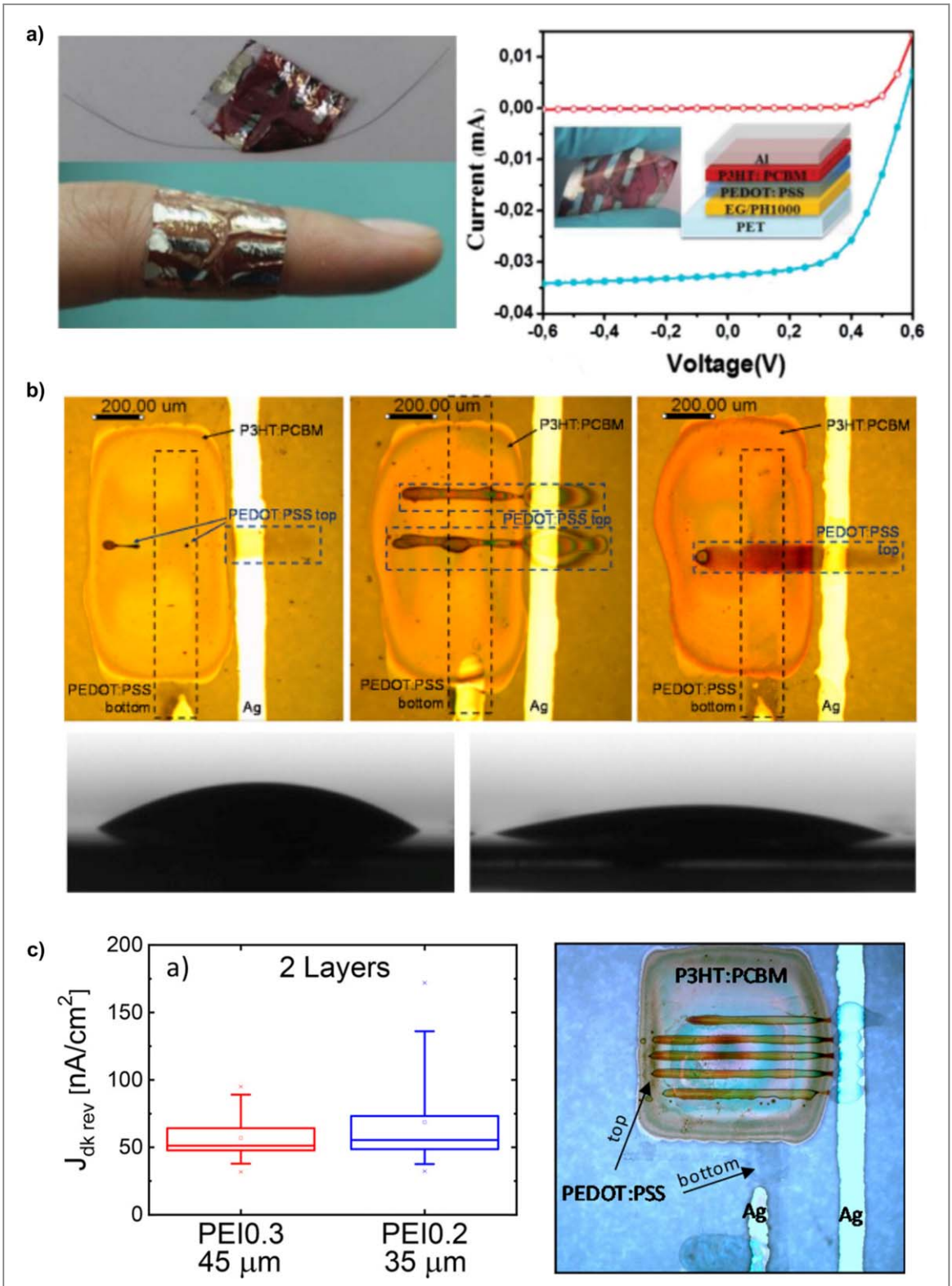

Figure 11. (a) Photograph and *IV*-curves of OPDs on ultra-thin PET foils with spray coated graphene:PEDOT electrodes. Reprinted with permission from [65], ©2014 WILEY-VCH Verlag GmbH & Co. KGaA, Weinheim. (b) Microscope images of inkjet printed OPDs without a poly-PT interlayer nor Zonyl as an additive (left), without poly-PT but with Zonyl (middle) and with poly-PT but without Zonyl (right). The bottom images show how poly-PT effectively reduces the contact angle of PEDOT on the P3HT:PCBM active layer. Reprinted with permission from [67], ©2016 Elsevier B.V. All rights reserved. (c) Statistics of dark current densities of OPDs with inkjet printed PEI layers from a multi solvent ink containing water, ethanol and ethylene glycol. The right micrograph shows the fabricated OPD. Reprinted with permission from [75], Copyright 2018 American Chemical Society.

deposition of PEDOT:PSS on the active layer [54]. However, when used on active layers the induced oxidation into the organic semiconductor might introduce damages and trapping sites at the interface which lead to a reduced device performance [94]. Therefore, some work has been devoted to investigating the use of interlayers, which facilitate the printing or coating of PEDOT:PSS. Aga *et al* showed how a drop cast layer of

a DNA prevents dewetting of aerosol jet printed PEDOT:PSS on a P3HT:PCBM layer [60]. While the printability was improved by this interlayer, the performance of the device was poor and did not show a clear diode rectification behavior. The authors attributed this to the ionic conductivity of the DNA. However, the choice of materials for the stack design also supports the conclusion of insufficient electron extraction and injection capabilities due to unfavorable energetic barriers. A very promising interlayer was tested by Grimoldi *et al* who used poly-PT for the simultaneous electron blocking and surface energy modification on top of a P3HT:PCBM layer in an inverted device architecture [67]. The layer was inkjet printed from a n-butanol:ethylene-glycol mixture (9:1) after careful ink formulation, which considered the solubility of poly-PT and the solvent orthogonality of the active materials. Furthermore, the high boiling point solvents prevented nozzle clogging and thus a stable printing process. Thanks to the presence of poly-PT the additive-free deposition of PEDOT:PSS was simplified due to a superior wettability as shown in figure 11(b).

In addition to the transparent hole extraction contact on the top, the inverted architecture further requires a low work function bottom electrode for the extraction of electrons. This issue can be resolved by the use of a printable materials such as Ag or PEDOT:PSS whose high WF is compensated by a suitable interlayer. The use of metal oxide films represents one of the most common approaches. Such films can either be cast from metal-organic precursor or nanoparticle based inks. Deposition of a TiO_x layer has been investigated through inkjet printing of a precursor solution in ethanol on top of ITO [78]. However, they encountered a strong coffee ring effect and had problems with nozzle clogging. Both issues could be traced back to the single low boiling point solvent ink. Strobel *et al* obtained smooth inkjet-printed ZnO layers from a nanoparticle ink using a solvent mixture of diethylene glycol and glycerol [35]. Another successful ink formulation was developed for aerosol jet printed Al-doped ZnO layers by the addition of mesitylene to a commercial nanoparticle ink [8]. Notably, this report allowed for the first demonstration of fully aerosol jet printed OPDs.

Another successful approach to lower the bottom electrode work function is the utilization of interfacial layers such as conjugated polyelectrolytes or amino functionalized conjugated polymers [95, 96]. Common examples for such materials are the polymers PEI or PEIE. However, to observe optimal results ultrathin layers below 10 nm are required which presents a big challenge for current printing techniques. The first non-spin coated realization of PEI layers for OPDs was reported utilizing spray coating to fabricate layers on ITO and PEDOT:PSS [63]. They showed how the work function could be lowered down to 4.1 eV by changing the concentration of the ink and the spraying time. Films of 20 nm thickness were eventually used for the fabrication of the first truly fully coated OPDs observing identical performance as spin coated references. Blade coating of PEIE layers on PEDOT:PSS was demonstrated shortly afterwards by Pierre *et al* resulting in a WF variation between 4.6 and 4.1 eV depending on the ink concentration [62]. Inkjet printing of PEI was only demonstrated very recently by Cesarini *et al* [75]. In their comprehensive study they found a suitable ink formulation of PEI yielding superior reproducibility of the OPD performance. They compared a single-solvent ink based on water to two multi-solvent inks containing water, ethanol and ethylene glycol. As expected, the single solvent ink resulted in poor device performance and yields below 20% due to layer inhomogeneities and issues in the jetting stability. The addition of ethanol and ethylene glycol served the purpose of increasing the boiling point to prevent nozzle failure and controlling ink viscosity after deposition to avoid coffee ring formation. A yield above 90% was achieved and the performance was considerably improved with reproducible dark currents in the range of 50 nA cm^{-2} as depicted in figure 11(c).

4.2.3. Surface pretreatments, patterning and encapsulation for printed OPDs

Beyond the design of device architecture and optimization of the device performance one should also consider industrially relevant processing steps that would be necessary to push printed OPDs toward a real-world application. These pre- or post-treatment approaches might facilitate the integration of more complex systems, help with device patterning, and/or enhance device functionality.

Pretreatment techniques often address the issue of the electrode structuring. This is especially important for coating techniques, which have no intrinsic lateral resolution. Several groups have reported the use of shadow masks for structuring electrodes as well as active layers through spray coating [61, 72]. For blade coating, the use of a plasma pre-treatment of the substrate through a stencil has been reported as an effective technique to obtain a selective wetting of the electrode material during the coating process [62, 76]. This method was furthermore used to fabricate an array of OPDs as shown in figure 12(a), which was employed in a 2D blood oximeter (see section 5 [80]. However, for both approaches the shadow mask constrains the achievable resolution, which in turn limits the possible integration density of devices. Furthermore, the use of masks prevents the free form fabrication of devices as any new design would require manufacturing a new mask. In this regard digital printing processes offer an inherent solution for this problem at the cost of longer fabrication times for large areas. The approach developed by Eckstein *et al* unites the strengths of high resolution and large area by combining the use of aerosol jet printing and area

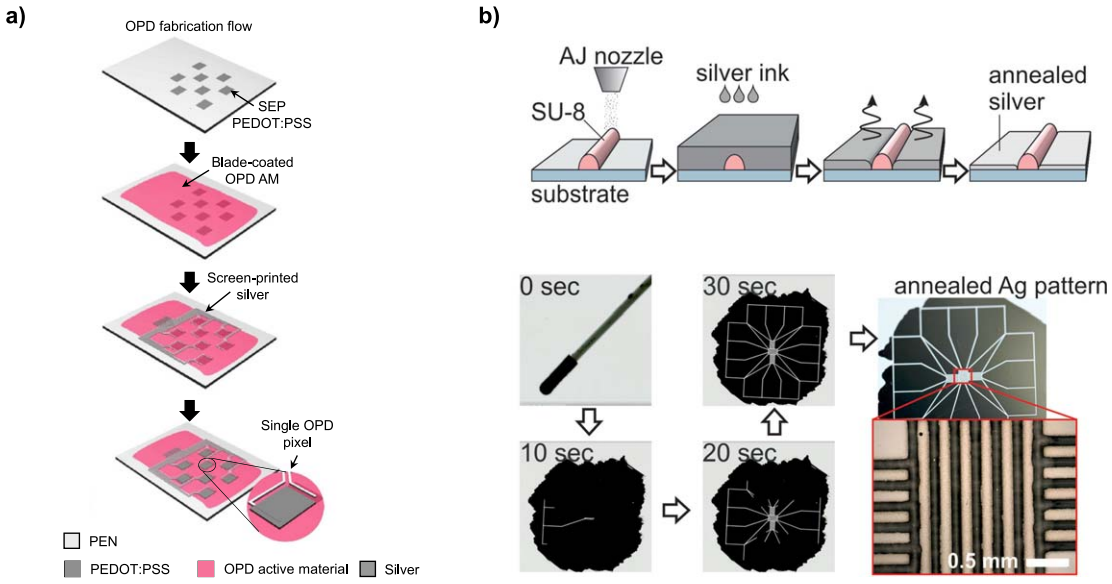

Figure 12. (a) OPD array fabrication through blade coating and screen printing. The bottom electrode is structured by an oxygen plasma pretreatment of the substrate to ensure selective wetting of the PEDOT ink. Reprinted with permission from [80], (Khan *et al* CC BY-NC-ND 2018). (b) Digital dewetting approach for self-assembly of electrode layouts through dewetting. An aerosol jet printed SU8 structure serves as a dewetting template which repels the subsequently deposited silver ink. Reprinted with permission from [66], ©2016 WILEY-VCH Verlag GmbH & Co. KGaA, Weinheim.

efficient techniques like inkjet, spray coating or blade coating [23]. For this purpose, the epoxy-based low surface-free-energy material (SU-8) was printed by aerosol jet followed by the homogeneous deposition of Ag ink by an arbitrary technique. After deposition, the SU-8 pattern provides a high surface free energy contrast compared to the substrate which guides the ink away from SU-8 and templates the electrode material in the desire layout as shown in figure 12(b). Furthermore, this technique offers full registration accuracy of all subsequently deposited device layers. This technique was used to fabricate single OPDs[23] as well as entire fully printed image sensors with 256 pixels and an individual pixel active area as low as 250 × 300 μm^2 [48].

Aside from the facilitation of OPD fabrication the substrate treatment may also enable an additional functionality of the final device. Falco *et al* reported on the use of a prestructured imprinted Ormostamp® substrate with a thin layer of evaporated aluminum to realize a wire grid polarizer [69]. On said polarizer a P3HT:PCBM OPD was spray coated. Simulations of this system predicted an extinction ratio between parallel and perpendicularly polarized light of more than 10^2. Characterization of fabricated devices successfully confirmed the predicted difference in $R(\lambda)$ for the respective polarization of light. However, the experimental data was merely able to reach a maximum extinction ratio of 50, which was attributed to the non-optimized parameters of the imprinting process and the nonlinearity of the response with light intensity. Nonetheless, the proof-of-concept is demonstrated and the application of such a polarization sensitive device can be envisioned in lab-on-a-chip architectures or for polarization multiplexing in optical communication.

After the fabrication of the OPD an encapsulation is necessary to ensure long term stability and functionality of the device. Most reports make use of curable adhesives and some kind of barrier material like glass or plastic foil. However, to ensure industrial relevance encapsulation techniques need to be developed which are sufficient for maintenance of OPD performance while not burdening the fabrication process. A first step in this direction is the combined process of e-beam evaporation of oxides and spray coating of poly(methyl methacrylate) (PMMA) [72]. With this encapsulation approach it was possible to maintain 40% of the photocurrent with the encapsulated device after two weeks, which was twice as much as the non-encapsulated reference.

5. OPD applications fabricated by industrial relevant printing and coating techniques

The demonstrated high performances of OPDs fabricated by industrially relevant coating and printing techniques has fueled the development of applications which benefits of these technologies in terms of additive integration and high-throughput.

Printed OPDs have been incorporated in lab-on-chip systems, as demonstrated by Wojciechowski *et al* [51]. In this example they fabricated a P3HT:PCBM based device on a cover slip through partial inkjet printing in combination with a handheld readout system that enabled the measurement of the photocurrent. The usability was demonstrated by the

detection of a chemiluminescent signal upon addition of a toxin. Detection levels down to 0.5 ng ml^{-1} were achieved with the system, which was comparable to the performance of CCD-based systems. The good response was attributed to the direct integration of the OPD on the cover slip considerably reducing the optical path of the luminescent signal without the need for additional optics. This advantage of reduced coupling losses was also exploited by Binda *et al* who spray coated a P3HT:PCBM OPD directly on the tip of an plastic optical fiber (POF) for optical communication in light-weight demanding applications [55]. Unfortunately, the device performance could not reach state-of-the-art FOMs of similar OPDs due to limited compatibility of the POF with the necessary annealing steps during device fabrication.

Both applications present above would furthermore benefit from the capability of spectral resolution. The reported spectrometer by Tang *et al* could be employed in this regard. They utilized the cavity enhanced narrow-band absorption explained in section 4.1.1 to fabricate a 1D array of OPDs with varying spectral responses by blade coating [83]. Through a positive gradient of the coating speed during active layer deposition, the thickness of the dried layer is increased along coating direction. Since the resonance frequency of the OPDs depend directly on the active layer thickness, the resulting wedge forms a spectrometer working in a wavelength range of 700–1100 nm. In their report, they demonstrated the functionality by recording the transmission spectrum of water in the NIR as an example for the application of such a system (see figure 13(a)).

A key feature of OPDs lies in the additive fabrication which enables facile integration onto multi-device electronic systems. The most basic and important example is the combination of OPDs with an amplification stage for an improved signal processing. While its integration with inorganic TFT-technology has been shown in several studies, the integration with a printed amplifier circuit based on organic field effect transistors (OFETs) has been demonstrated by Maiellaro *et al.* The P3HT:PCBM OPD and the operational amplifier based on n- and p-type semiconductors (Polyera ActiveInk and TIPS-pentacene) were fabricated partially by printing techniques on two separate foils which were glued together with a conductive adhesive to ensure electrical connection. The output current of the OPD in the range of 1–3 μA was successfully amplified to an output voltage range of 0.7–2 V through the use of a feedback resistor of 680 kΩ [58].

Another example for an integrated printed circuit comprising of a printed OPD is reported by Dell'Erba *et al* [97]. They fabricated a twilight switch on the basis of a Schmitt-trigger and an OPD through the use of a combination of inkjet printing and bar coating. The final system, which is shown in figure 13(b) outputs a digital ON/OFF signal depending on the illumination intensity. The Schmitt-trigger circuitry allowed for the setting of two thresholds for ON (P_{T+}) and OFF (P_{T-}) signals, which improved the system stability in regard to intensity fluctuations during dusk or dawn. Necessary n- and p-type OFETs are fabricated from P(NDI2OD)-T2 and diketopyrrolopyrrole-thieno [3,2-b]tiophene (DPPT-TT). The P3HT:PCBM OPD was structured in a lateral architecture as this provided a larger electrode distance and a reduced electric field caused by the high bias voltage necessary for the operation of the Schmitt-trigger. Rectification behavior is achieved by depositing PFN on one of the two PEDOT electrodes as a work function modifying layer. The functionality of the system was demonstrated by stepwise illumination intensity increase leading to a switching of the output voltage after passing the respective ON and OFF thresholds.

Aside from the detection side of an optical system one should consider the necessary elements for the electronic readout of the measured signal. A connection by cables may limit the use of OPDs in many applications like wearable devices or mobile sensors, therefore wireless communication circuits utilizing RFID technology are of great interest in this regard. Such a system has been fabricated by inkjet printing an RF antenna as well as the necessary contact lines, spray coating a P3HT:PCBM OPD and integrating a Silicon RFID chip through the use of a conductive adhesive [71]. The obtained system was capable of measuring illumination intensities down to 1.3 μW cm^{-2} utilizing a high feedback resistor with a read range of 80 cm between the tag and the commercial RFID reader.

The application of OPDs in medical sensors is especially interesting due to their potential compatibility to soft materials and tunability of spectral range. One of the most prominent applications of OPDs in recent publications has been the fabrication of blood oximeters comprising of organic electronic devices. Lochner *et al* were the first to report a partially blade coated PTB7:PC70BM OPD on a flexible PEN substrate for this purpose [11]. In combination with two separately fabricated red and green OLEDs the change in absorption of the oxygenated blood flowing through a fingertip could be measured. From the ratio of the red and green absorption it is possible to calculate the blood oxygenation level. In comparison with a commercial inorganic pulse oximeter, the oxygenation level only had an error of 2%. Another example showing a pulse oximeter in reflection mode was recently demonstrated by the same group, allowing for a higher versatility on the location of measurement [80]. Aside from the new mode of operation, the system was further improved by replacing the green OLED with a NIR OLED and by mounting multiple devices in an array like architecture as shown in figure 14(a). The use of the NIR OLED makes use of the higher transmission of the skin in this regime to increase the signal reaching the OPDs. Interestingly, the array structure enables 2D mapping of the oxygenation of the skin as well as the detection of changes in

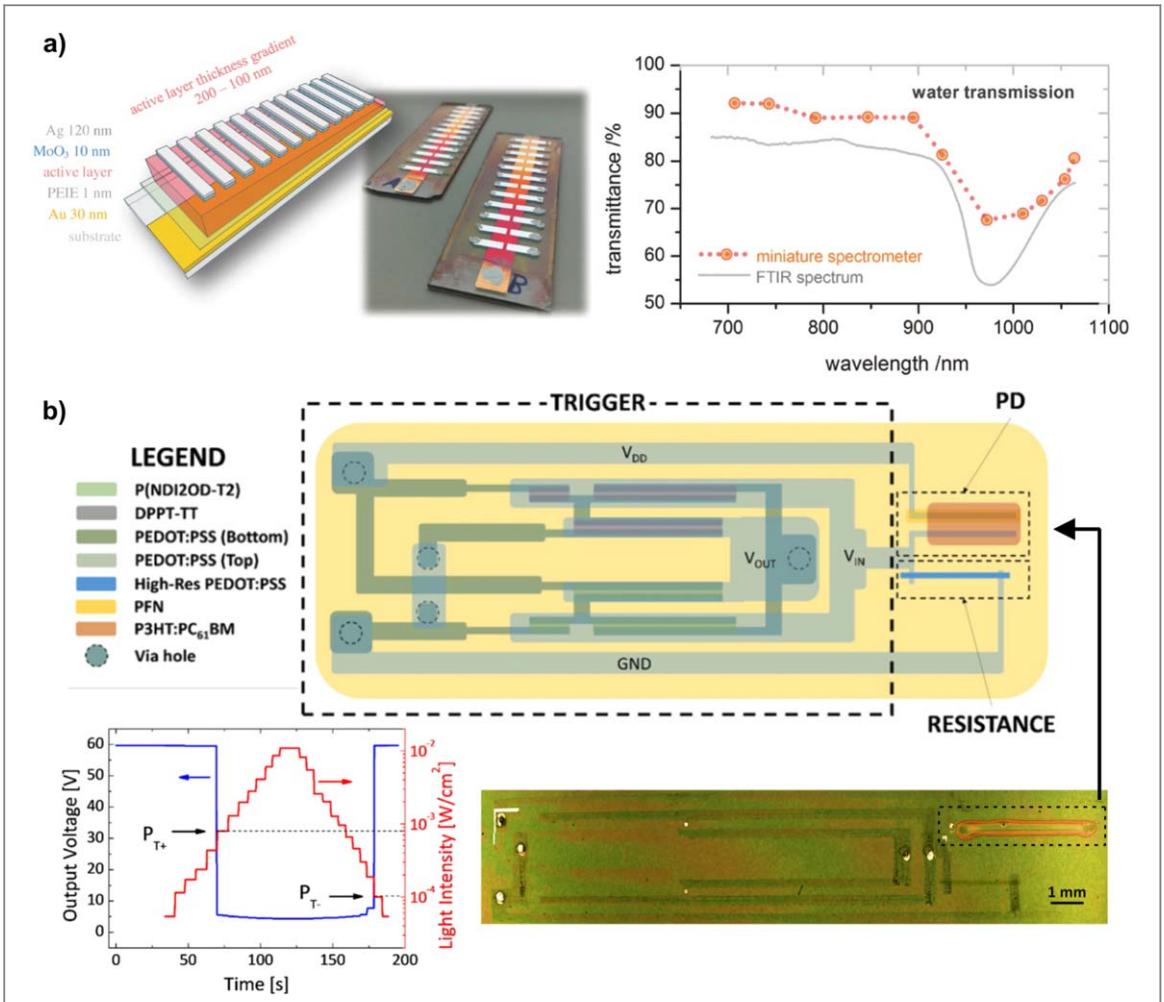

Figure 13. (a) Blade coated miniature spectrometer based on cavity enhanced charge transfer state absorption. The narrow NIR response allows for the measurement of the IR-transmission spectrum of water. Reprinted with permission from [83], ©2017 WILEY-VCH Verlag GmbH & Co. KGaA, Weinheim. (b) Fully printed twilight switch based on a Schmitt-trigger circuit and a lateral P3HT:PCBM OPD. The output voltage of the system switches between ON and OFF depending on the illumination intensity, once the thresholds P_{T+} and P_{T-} are reached. Reprinted with permission from [97], ©2015 IOP Publishing Ltd

the oxygenation, when pulsatile blood flow is restricted or very low. The devices were fabricated mainly by blade coating except for top silver or aluminum electrodes which were screen printed or evaporated, respectively. Since blade coating limits the structural flexibility of the fabricated devices, the OLEDs and OPDs had to be fabricated on three separate substrates, which were later combined to form the entire system. In the future one could imagine an integration of the various devices on the same substrate through additive non-contact printing techniques, which would considerably simplify the process and mechanical flexibility of the system due to a reduced thickness.

Another application with great potential for medical diagnosis and industrial or consumer electronic systems are 2D image sensors. Organic materials provide characteristics that enhance current systems such as mechanical flexibility, tunable absorption and large area processability. The current examples of OPD-based image sensors often comprise of a pixel array connected to an inorganic backplane providing the necessary circuitry. In this configuration every pixel is read individually by at least one transistor. Typically, the OPD is processed homogeneously by coating techniques while the pixels are defined by the amorphous Silicon [15, 64, 81], amorphous Indium gallium zinc oxide (IGZO) [9] or CMOS backplane [54]. The deposition of the active layers has been limited to coating techniques including blade coating [15], slot-die coating [9] and most prominently spray coating [15, 54, 64]. The capability of the latter to fabricate thick layers was utilized by Büchele *et al* to process a blend of P3HT:PCBM and scintillator microparticles to enable x-ray imaging. The integration of the scintillator in the active layer of the OPD improved the imaging resolution by more than a factor of two compared to the stacked architecture with the scintillator on top of the OPD. The modulation transfer function dropped to 0.2 at 4.74 line-pairs per mm (lp mm^{-1}). This is a typical value for image sensor systems employing a-Si backplanes having pixel sizes in the range of 100 μm [15, 81]. Akkerman *et al* have shown an increase in the resolution through the use of an IGZO backplane which suffers less from pixel crosstalk and

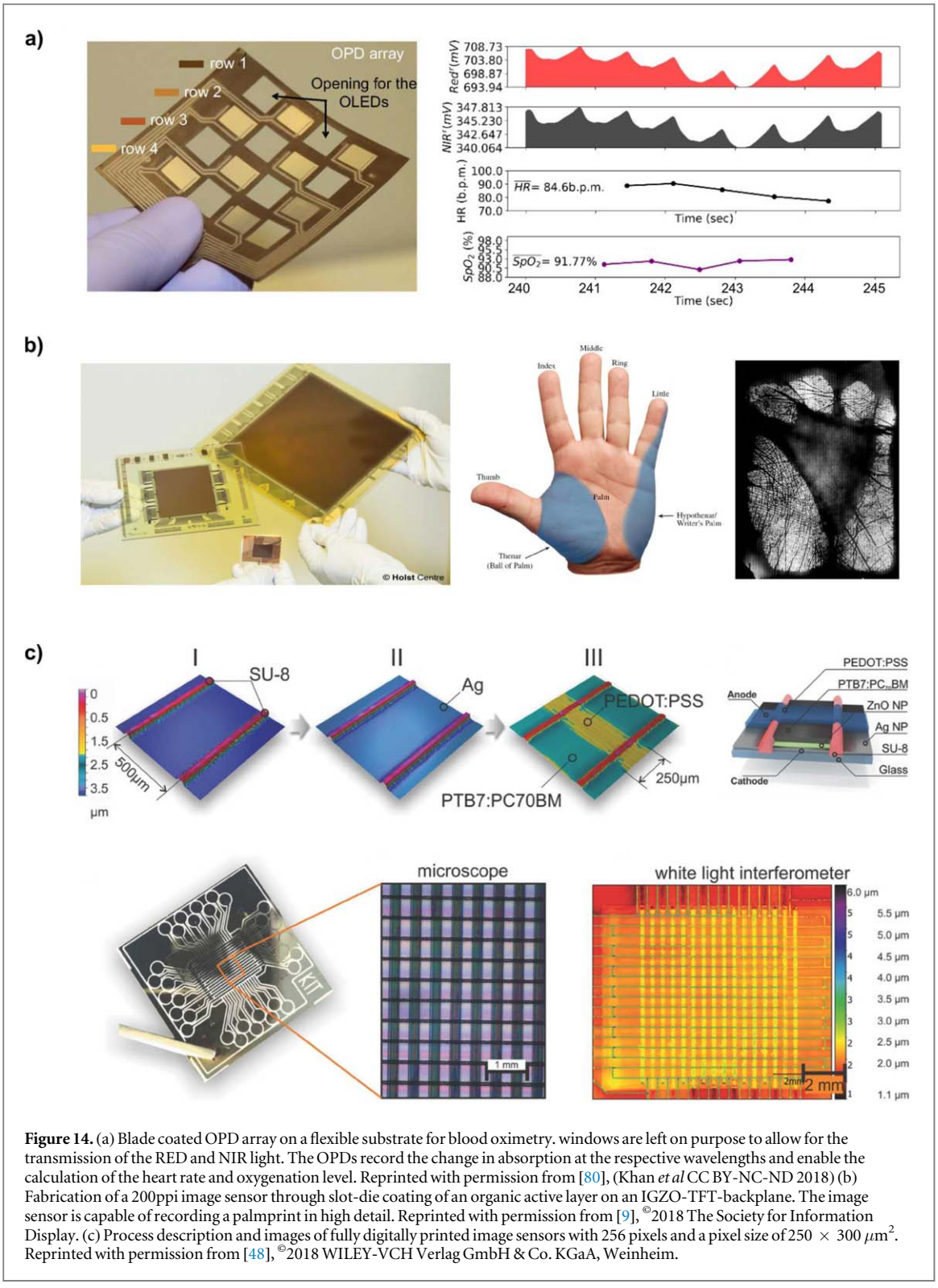

Figure 14. (a) Blade coated OPD array on a flexible substrate for blood oximetry. windows are left on purpose to allow for the transmission of the RED and NIR light. The OPDs record the change in absorption at the respective wavelengths and enable the calculation of the heart rate and oxygenation level. Reprinted with permission from [80], (Khan *et al* CC BY-NC-ND 2018) (b) Fabrication of a 200ppi image sensor through slot-die coating of an organic active layer on an IGZO-TFT-backplane. The image sensor is capable of recording a palmprint in high detail. Reprinted with permission from [9], ©2018 The Society for Information Display. (c) Process description and images of fully digitally printed image sensors with 256 pixels and a pixel size of 250 × 300 μm^2. Reprinted with permission from [48], ©2018 WILEY-VCH Verlag GmbH & Co. KGaA, Weinheim.

reached up to 11 lp mm^{-1} although having a larger pixel footprint ~125 μm. The 200ppi image sensor with 480 × 640 pixels is shown in figure 14(b). It was capable of recording the print of a human hand enabling application for identification and security purposes [9].

While it is in principle possible to fabricate a backplane through printing and coating, a fully printed image sensor with on-pixel transistors has not been demonstrated yet. However, a fully printed passive read out image sensor was reported recently by Eckstein *et al* [48]. They fabricated an OPD array with the help of the previously mentioned dewetting approach utilizing an aerosol jet printed SU8-template [66]. The active materials including silver, ZnO, PTB7:PC70BM and PEDOT:PSS are deposited through a combination of inkjet and aerosol jet printing to form a functional image sensor with 256 pixels and a pixel size of

250 × 300 μm^2 each. Figure 14(c) displays the fabrication process and the final image sensor. Characterization of the separate OPDs showed high performance homogeneity and a fabrication yield of 100%. This consistency was attributed to the benefit of the dewetting approach which limits material displacement and enable a perfect registration accuracy of the stacked layers. Imaging capabilities were demonstrated by recording the illumination through various shadow masks and digitizing the signals with an Arduino based readout circuit. The main drawback of the passive read out system was found to be the electronic cross talk resulting from ring currents due to the shared electrode lines. This could be overcome in the future if on-pixel transistors are implemented for signal readout.

6. Conclusions and outlook

The development and performance of OPDs processed by industrially relevant printing and coating techniques have seen tremendous advancements in the last decade. Devices exhibiting $R(\lambda)$ responsivities >400 mA W^{-1} and specific Detectivities $>10^{13}$ Jones over wavelength ranges from visible to NIR have been reported as well as devices with detection speeds >2 MHz. These FOM render OPD technologies suitable for the development of technological and commercial applications some of them already being demonstrated in the form of integrated sensor systems, functional imagers or pulse oximeters. While a variety of fabrication methods are employed, Inkjet printing, and spray coating stand out as the most commonly used research techniques, promising digital freedom of design and large-area fabrication. However, various challenges still remain, few fully printed examples have been demonstrated to date as the inherent difficulties of printing multilayer devices are still being addressed through ink formulation and material choice. Additionally, we found that most of the printed OPD research utilizes materials optimized for broad band solar applications, therefore we expect future research to take hand of the enormous pallet of organic semiconductors to simultaneously address the diversification of application fields and solving printing related problems. Particularly, it is expected that the current trend in development of IR sensitive materials will be transferred into printed applications. Furthermore, printable device concepts allowing for a narrow optical response or light management in combination with printed optics are expected to strongly develop in the near future. Lastly, it is noteworthy that very few studies report lifetime tests which ultimately define the application setting of the device. This could be in part due to the symptomatic lack of common characterization standards in the OPD field which is currently being addressed by some of the leading research groups. In summary, we believe that printing and coating techniques will enable the integration and rapid development of optical sensor systems. Specially, we think that they can provide the cost-efficiency, versatility, additive manufacturing and high-throughput requirements for the development of applications in the area of disposable medical sensors and internet-of-things technologies.

Acknowledgments

The authors acknowledge the support of the Federal Ministry for Education and Research (BMBF) through Grant No. 13N13691. MS is grateful for the financial support and mentoring from the German Academic Scholarship Foundation. The data in figure 7(a) was obtained by digitizing graphs from the cited literature with the open source software Engauge Digitizer [98].

ORCID iDs

Gerardo Hernandez-Sosa https://orcid.org/0000-0002-2871-6401

References

[1] García de Arquer F P, Armin A, Meredith P and Sargent E H 2017 Solution-processed semiconductors for next-generation photodetectors nature reviews *Materials* **2** 16100
[2] Kielar M, Dhez O, Pecastaings G, Curutchet A and Hirsch L 2016 Long-term stable organic photodetectors with ultra low dark currents for high detectivity applications *Sci. Rep.* **6** 39201
[3] Wu Z, Yao W, London A E, Azoulay J D and Ng T N 2018 Elucidating the detectivity limits in shortwave infrared organic photodiodes *Adv. Funct. Mater.* **28** 1800391
[4] Liu X, Lin Y, Liao Y, Wu J and Zheng Y 2018 Recent advances in organic near-infrared photodiodes *J. Mater. Chem.* C **6** 3499–513
[5] Yang D and Ma D 2018 Development of organic semiconductor photodetectors: from mechanism to applications advanced *Opt. Mater.* **7** 1800522
[6] Azzellino G, Grimoldi A, Binda M, Caironi M, Natali D and Sampietro M 2013 Fully inkjet-printed organic photodetectors with high quantum yield *Adv. Mater.* **25** 6829–33
[7] Pace G, Grimoldi A, Sampietro M, Natali D and Caironi M 2015 Printed photodetectors *Semicond. Sci. Technol.* **30** 104006
[8] Eckstein R, Rödlmeier T, Glaser T, Valouch S, Mauer R, Lemmer U and Hernandez-Sosa G 2015 Aerosol-jet printed flexible organic photodiodes: semi-transparent, color neutral, and highly efficient *Adv. Electron. Mater.* **1** 1500101
[9] Akkerman H *et al* 2018 39-3: Printed organic photodetector arrays and their use *Palmprint Scanners SID Symp. Digest of Technical Papers* vol 49, pp 494–7
[10] Jansen-van Vuuren R D, Armin A, Pandey A K, Burn P L and Meredith P 2016 Organic photodiodes: the future of full color detection and image sensing *Adv. Mater.* **28** 4766–802
[11] Lochner C M, Khan Y, Pierre A and Arias A C 2014 All-organic optoelectronic sensor for pulse oximetry *Nat. Commun.* **5** 5745
[12] Khan Y, Ostfeld A E, Lochner C M, Pierre A and Arias A C 2016 Monitoring of vital signs with flexible and wearable medical devices *Adv. Mater.* **28** 4373–95
[13] Bansal A K, Hou S, Kulyk O, Bowman E M and Samuel I D W 2015 Wearable organic optoelectronic sensors for medicine *Adv. Mater.* **27** 7638–44
[14] Xu X, Davanco M, Qi X and Forrest S R 2008 Direct transfer patterning on three dimensionally deformed surfaces at

micrometer resolutions and its application to hemispherical focal plane detector arrays *Org. Electron.* **9** 1122–7
[15] Gasparini N, Gregori A, Salvador M, Biele M, Wadsworth A, Tedde S, Baran D, McCulloch I and Brabec C J 2018 Visible and near-infrared imaging with nonfullerene-based photodetectors *Adv. Mater. Technol.* **3** 1800104
[16] Vega-Colado C *et al* 2018 An all-organic flexible visible light communication system *Sensors* **18** 3045
[17] Smith S, Korvink J G, Mager D and Land K 2018 The potential of paper-based diagnostics to meet the ASSURED criteria *RSC Adv.* **8** 34012–34
[18] Lee S, Kim H and Kim Y 2019 Multistacked detectors with transparency-controlled polymer:nonfullerene bulk heterojunction sensing layers for visible light communications *ACS Omega* **4** 3611–8
[19] Lee Y *et al* 2018 Stretchable organic optoelectronic sensorimotor synapse *Sci. Adv.* **4** eaat7387
[20] Baeg K-J, Binda M, Natali D, Caironi M and Noh Y-Y 2013 Organic light detectors: photodiodes and phototransistors *Adv. Mater.* **25** 4267–95
[21] Oliveira J, Brito-Pereira R, Gonçalves B F, Etxebarria I and Lanceros-Mendez S 2019 Recent developments on printed photodetectors for large area and flexible applications *Org. Electron.* **66** 216–26
[22] Bredas J-L 2017 Organic electronics: Does a plot of the HOMO–LUMO wave functions provide useful information? *Chem. Mater.* **29** 477–8
[23] Eckstein R and Lemmer U 2016 *Aerosol Jet Printed Electronic Devices and Systems* (Karlsruhe: KIT-Bibliothek)
[24] Armin A, Jansen-van Vuuren R D, Kopidakis N, Burn P L and Meredith P 2015 Narrowband light detection via internal quantum efficiency manipulation of organic photodiodes *Nat. Commun.* **6** 6343
[25] Roth B, Søndergaard R R and Krebs F C 2015 7-Roll-to-roll printing and coating techniques for manufacturing large-area flexible organic electronics *Handbook of Flexible Organic Electronics* ed S Logothetidis (Oxford: Woodhead) pp 171–97
[26] Merklein L *et al* 2019 Comparative study of printed multilayer OLED fabrication through slot die coating, gravure and inkjet printing, and their combination colloids and interfaces *Colloids Interfaces* **3** 32
[27] Grau G, Cen J, Kang H, Kitsomboonloha R, Scheideler W J and Subramanian V 2016 Gravure-printed electronics: recent progress in tooling development, understanding of printing physics, and realization of printed devices *Flex. Print. Electron.* **1** 023002
[28] Hernandez-Sosa G, Bornemann N, Ringle I, Agari M, Dörsam E, Mechau N and Lemmer U 2013 Rheological and drying considerations for uniformly gravure-printed layers: towards large-area flexible organic light-emitting diodes *Adv. Funct. Mater.* **23** 3164–71
[29] Katz E A, Mescheloff A, Visoly-Fisher I and Galagan Y 2016 Light intensity dependence of external quantum efficiency of fresh and degraded organic photovoltaics *Sol. Energy Mater. Sol. Cells* **144** 273–80
[30] Fang Y, Armin A, Meredith P and Huang J 2019 Accurate characterization of next-generation thin-film photodetectors *Nat. Photon.* **13** 1–4
[31] Johnson J B 1925 The Schottky effect in low frequency circuits *Phys. Rev.* **26** 71–85
[32] Schottky W 1926 Small-shot effect and flicker effect *Phys. Rev.* **28** 74–103
[33] Jones R C 1959 Noise in radiation detectors *Proc. IRE* **47** 1481–6
[34] Kolanoski H and Wermes N 2016 17 Signalverarbeitung und Rauschen *Teilchendetektoren* (Berlin: Springer) pp 719–805
[35] Strobel N, Seiberlich M, Rödlmeier T, Lemmer U and Hernandez-Sosa G 2018 Non-fullerene-based printed organic photodiodes with high responsivity and megahertz detection speed *ACS Appl. Mater. Interfaces* **10** 42733–9
[36] Blackman R B, Ralph B, Tukey J W and John W 1959 *The Measurement of Power spectra From the Point of View of Communications Engineering* (New York: Dover)
[37] Jones R C 1952 'Detectivity': the reciprocal of noise equivalent input of radiation *Nature* **170** 937
[38] Jones R C 1960 Proposal of the detectivity D** for detectors limited by radiation noise† *J. Opt. Soc. Am.* **50** 1058–9
[39] Kato K, Hata S, Yoshida J and Kozen A 1992 Design of high-speed and high-sensitivity photodiode with an input optical waveguide on semi-insulating InP substrate *LEOS 1992 Summer Topical Meeting Digest on Broadband Analog and Digital Optoelectronics, Optical Multiple Access Networks, Integrated Optoelectronics, and Smart Pixels* pp 254–7
[40] Sullivan T, Middleman S and Keunings R 1987 Use of a finite-element method to interpret rheological effects in blade coating *AlChE J.* **33** 2047–56
[41] Aidun C K and Triantafillopoulos N G 1997 *High-Speed Blade Coating Liquid Film Coating: Scientific Principles and their Technological Implications* ed S F Kistler and P M Schweizer (Berlin: Springer) pp 637–72
[42] Patil P S 1999 Versatility of chemical spray pyrolysis technique *Mater. Chem. Phys.* **59** 185–98
[43] Montenegro Benavides C, Rechberger S, Spiecker E, Berlinghof M, Unruh T, Biele M, Schmidt O, Brabec C J and Tedde S F 2018 Improving spray coated organic photodetectors performance by using 1,8-diiodooctane as processing additive *Org. Electron.* **54** 21–6
[44] Machui F *et al* 2014 Cost analysis of roll-to-roll fabricated ITO free single and tandem organic solar modules based on data from manufacture *Energy Environ. Sci.* **7** 2792–802
[45] Sandström A and Edman L 2015 Towards high-throughput coating and printing of light-emitting electrochemical cells: a review and cost analysis of current and future *Methods Energy Technology* **3** 329–39
[46] Kipphan H 2000 *Handbuch der Printmedien: Technologien und Produktionsverfahren* (Berlin: Springer)
[47] García F J, González H, Castrejón-Pita J R and Castrejón-Pita A A 2014 The breakup length of harmonically stimulated capillary jets *Appl. Phys. Lett.* **105** 094104
[48] Eckstein R, Strobel N, Rödlmeier T, Glaser K, Lemmer U and Hernandez-Sosa G 2018 Fully digitally printed image sensor based on organic photodiodes *Adv. Opt. Mater.* **6** 1701108
[49] Agarwala S, Goh G L and Yeong W Y 2017 Optimizing aerosol jet printing process of silver ink for printed electronics *IOP Conf. Ser.: Mater. Sci. Eng.* **191** 012027
[50] Tedde S F, Kern J, Sterzl T, Fürst J, Lugli P and Hayden O 2009 Fully spray coated organic photodiodes *Nano Lett.* **9** 980–3
[51] Wojciechowski J R, Shriver-Lake L C, Yamaguchi M Y, Füreder E, Pieler R, Schamesberger M, Winder C, Prall H J, Sonnleitner M and Ligler F S 2009 Organic photodiodes for biosensor miniaturization *Anal. Chem.* **81** 3455–61
[52] Lavery L L, Whiting G L and Arias A C 2011 All ink-jet printed polyfluorene photosensor for high illuminance detection *Org. Electron.* **12** 682–5
[53] Lilliu S, Böberl M, Sramek M, Tedde S F, Macdonald J E and Hayden O 2011 Inkjet-printed organic photodiodes *Thin Solid Films* **520** 610–5
[54] Baierl D, Pancheri L, Schmidt M, Stoppa D, Dalla Betta G-F, Scarpa G and Lugli P 2012 A hybrid CMOS-imager with a solution-processable polymer as photoactive layer *Nat. Commun.* **3**
[55] Binda M, Natali D, Iacchetti A and Sampietro M 2013 Integration of an organic photodetector onto a plastic optical fiber by means of spray coating technique *Adv. Mater.* **25** 4335–9
[56] Saracco E, Bouthinon B, Verilhac J-M, Celle C, Chevalier N, Mariolle D, Dhez O and Simonato J-P 2013 Work function tuning for high-performance solution-processed organic photodetectors with inverted structure *Adv. Mater.* **25** 6534–8
[57] Pace G, Grimoldi A, Natali D, Sampietro M, Coughlin J E, Bazan G C and Caironi M 2014 All-organic and fully-printed semitransparent photodetectors based on narrow bandgap conjugated molecules *Adv. Mater.* **26** 6773–7
[58] Maiellaro G, Ragonese E, Gwoziecki R, Jacobs S, Marjanović N, Chrapa M, Schleuniger J and Palmisano G 2014 Ambient light organic sensor in a printed complementary

organic tft technology on flexible plastic foil *IEEE Trans. Circuits Syst.* I **61** 1036–43
[59] Falco A, Cinà L, Scarpa G, Lugli P and Abdellah A 2014 Fully-sprayed and flexible organic photodiodes with transparent carbon nanotube electrodes *ACS Appl. Mater. Interfaces* **6** 10593–601
[60] Aga R S, Lombardi J P, Bartsch C M and Heckman E M 2014 Performance of a printed photodetector on a paper substrate *IEEE Photonics Technol. Lett.* **26** 305–8
[61] Schmidt M, Falco A, Loch M, Lugli P and Scarpa G 2014 Spray coated indium-tin-oxide-free organic photodiodes with PEDOT:PSS anodes *AIP Adv.* **4** 107132
[62] Pierre A, Deckman I, Lechêne P B and Arias A C 2015 High detectivity all-printed organic photodiodes *Adv. Mater.* **27** 6411–7
[63] Falco A, Zaidi A M, Lugli P and Abdellah A 2015 Spray deposition of polyethylenimine thin films for the fabrication of fully-sprayed organic photodiodes *Org. Electron.* **23** 186–92
[64] Büchele P *et al* 2015 X-ray imaging with scintillator-sensitized hybrid organic photodetectors *Nat. Photon.* **9** 843–848
[65] Liu Z, Parvez K, Li R, Dong R, Feng X and Müllen K 2015 Transparent conductive electrodes from graphene/PEDOT: PSS hybrid inks for ultrathin organic photodetectors *Adv. Mater.* **27** 669–75
[66] Eckstein R, Alt M, Rödlmeier T, Scharfer P, Lemmer U and Hernandez-Sosa G 2016 Digitally printed dewetting patterns for self-organized microelectronics *Adv. Mater.* **28** 7708–15
[67] Grimoldi A, Colella L, La Monaca L, Azzellino G, Caironi M, Bertarelli C, Natali D and Sampietro M 2016 Inkjet printed polymeric electron blocking and surface energy modifying layer for low dark current organic photodetectors *Org. Electron.* **36** 29–34
[68] Abdellah A, Falco A, Schwarzenberger U, Scarpa G and Lugli P 2016 Transfer printed P3HT/PCBM photoactive layers: from material intermixing to device characteristics *ACS Appl. Mater. Interfaces* **8** 2644–51
[69] Falco A, Nagel R, Lugli P, Bezzeccheri E, Liguori R and Rubino A 2016 Simulation and fabrication of polarized organic photodiodes *2016 IEEE Sensors* pp 1–3
[70] Kim H, Moon J, Lee K and Kanicki J 2017 3D printed masks and transfer stamping process to enable the fabrication of the hemispherical organic photodiodes *Adv. Mater. Technol.* **2** 1700090
[71] Falco A, Salmerón J F, Loghin F C, Lugli P and Rivadeneyra A 2017 Fully printed flexible single-chip RFID tag with light detection capabilities *Sensors* **17** 534
[72] Falco A, Lugli P, Loghin F C, Bobinger M and Gerlt M 2017 Spray deposition of polymeric thin-films for the inline encapsulation of organic photodiodes *2017 IEEE 17th Int. Conf. on Nanotechnology (IEEE-NANO)* pp 522–5
[73] Kim H, Song B, Lee K, Forrest S and Kanicki J 2017 Bilayer interdiffused heterojunction organic photodiodes fabricated by double transfer stamping *Adv. Opt. Mater.* **5** 1600784
[74] Shu Z, Kemper F, Beckert E, Eberhardt R and Tünnermann A 2017 Highly sensitive on-chip fluorescence sensor with integrated fully solution processed organic light sources and detectors *RSC Adv.* **7** 26384–91
[75] Cesarini M, Brigante B, Caironi M and Natali D 2018 Reproducible, high performance fully printed photodiodes on flexible substrates through the use of a polyethylenimine interlayer *ACS Appl. Mater. Interfaces* **10** 32380–6
[76] Deckman I, Lechêne P B, Pierre A and Arias A C 2018 All-printed full-color pixel organic photodiode array with a single active layer *Org. Electron.* **56** 139–45
[77] Jang W and Wang D H 2018 Long-term stable transferred organic photoactive layer-based photodiode with controlled wetting through interface stabilization *ACS Appl. Mater. Interfaces* **10** 38603–9
[78] Cherian D, Mitra K Y, Hartwig M, Malinowski P E and Baumann R R 2018 Fabrication of organic photo detectors using inkjet technology and its comparison to conventional deposition processes *IEEE Sens. J.* **18** 94–105
[79] Yen C-T, Huang Y-C, Yu Z-L, Cha H-C, Hsiao H-T, Liang Y-T, Chien F S-S and Tsao C-S 2018 Performance improvement and characterization of spray-coated organic photodetectors *ACS Appl. Mater. Interfaces* **10** 33399–406
[80] Khan Y *et al* 2018 A flexible organic reflectance oximeter array *Proc. Natl Acad. Soc.* **115** E11015–24
[81] Biele M, Benavides C M, Hürdler J, Tedde S F, Brabec C J and Schmidt O 2019 Spray-coated organic photodetectors and image sensors with silicon-like performance *Adv. Mater. Technol.* **4** 1800158
[82] Wang X, Wang J, Zhao H, Jin H and Yu J 2019 Detectivity enhancement of double-layer organic photodetectors consisting of solution-processed interconnecting layers *Mater. Lett.* **243** 81–3
[83] Tang Z *et al* 2017 Polymer:fullerene bimolecular crystals for near-infrared spectroscopic photodetectors *Adv. Mater.* **29** 1702184
[84] Koetse M M, Rensing P A, van Heck G T, Meulendijks N N M M, Kruijt P G M, Enting E H, Wieringa F P and Schoo H F M 2008 Optical sensor platforms by modular assembly of organic electronic devices *2008 IEEE Sensors Applications Symp.* pp 1–3
[85] Hou J, Inganäs O, Friend R H and Gao F 2018 Organic solar cells based on non-fullerene acceptors *Nat. Mater.* **17** 119–28
[86] Yang Y, Omi S, Goto R, Yahiro M, Era M, Watanabe H and Oki Y 2011 Wavelength sensitive photodiodes in the visible based on J-type aggregated films patterned by inkjet method *Org. Electron.* **12** 405–10
[87] Yang Y, Nakamichi T, Yoshioka H, Yahiro M, Era M, Watanabe H, Cui Y, Oki Y and Qian G 2013 Spectral-resolving capable and integratable multilayered conductive films via an inkjet method *J. Mater. Chem.* C **1** 1739–44
[88] Nakamichi T, Yang Y, Ohta T, Yoshioka H, Yahiro M, Era M, Watanabe H, Cui Y, Oki Y and Qian G 2013 Stackable spectral-sensitive conductive films based on cyanine aggregates via an inkjet method *Dyes Pigments* **98** 333–8
[89] Strobel N, Eckstein R, Lehr J, Lemmer U and Hernandez-Sosa G 2018 Semiconductor:insulator blends for speed enhancement in organic photodiodes *Adv. Electron. Mater.* **4** 1700345
[90] Yang Y, Nakamichi T, Yoshioka H, Omi S, Goto R, Watanabe H and Oki Y 2011 Intensity sensitive organic photodiodes patterned by inkjet method *Mol. Cryst. Liq. Cryst.* **538** 136–42
[91] Hoth N C, Choulis A S, Schilinsky P and Brabec J C 2009 On the effect of poly(3-hexylthiophene) regioregularity on inkjet printed organic solar cells *J. Mater. Chem.* **19** 5398–404
[92] Huang Y, Wen W, Mukherjee S, Ade H, Kramer E J and Bazan G C 2014 High-molecular-weight insulating polymers can improve the performance of molecular solar cells *Adv. Mater.* **26** 4168–72
[93] Lamont C A, Eggenhuisen T M, Coenen M J J, Slaats T W L, Andriessen R and Groen P 2015 Tuning the viscosity of halogen free bulk heterojunction inks for inkjet printed organic solar cells *Org. Electron.* **17** 107–14
[94] Baierl D, Fabel B, Lugli P and Scarpa G 2011 Efficient indium-tin-oxide (ITO) free top-absorbing organic photodetector with highly transparent polymer top electrode *Org. Electron.* **12** 1669–73
[95] Hoven C V, Garcia A, Bazan G C and Nguyen T-Q 2008 Recent applications of conjugated polyelectrolytes in optoelectronic devices *Adv. Mater.* **20** 3793–810
[96] Guan X, Zhang K, Huang F, Bazan G C and Cao Y 2012 Amino N-oxide functionalized conjugated polymers and their amino-functionalized precursors: new cathode interlayers for high-performance optoelectronic devices *Adv. Funct. Mater.* **22** 2846–54
[97] Dell'Erba G, Perinot A, Grimoldi A, Natali D and Caironi M 2015 Fully-printed, all-polymer integrated twilight switch *Semicond. Sci. Technol.* **30** 104005
[98] Mitchell M 2019 markummitchell/engauge-digitizer: New point types https://zenodo.org/record/3370364#.XdU29HHgphE